Supporting Information

Theoretical Guidance and Feedback on the Design, Preparation, and Efficient Catalytic Oxidation of Novel Imidazole-Modified Iron Porphyrin Catalysts

Shaojuan Chen[a,b,c], Yaojie Liu[a,b,c,d], Kun Liu[a,b,c], Mo xian[a,b,c], Zhiyi Xu[a,b,c], Long Jiang[a,b,c], Weizhi Sun[e], Zongjiang Yu[a,b,c], * Chao Xu [a,b,c], *

[a] *CAS Key Laboratory of Biobased Materials, Qingdao Institute of Bioenergy and Bioprocess Technology, Chinese Academy of Sciences, Qingdao 266101, China*

[b] *Shandong Energy Institute, Qingdao 266101, China*

[c] *Qingdao New Energy Shandong Laboratory, Qingdao 266101, China*

[d] *State Key Laboratory Base of Eco-chemical Engineering, College of Chemical Engineering, Qingdao University of Science and Technology, Qingdao 266101, China*

[e] *Dalian Institute of Chemical Physics, Chinese Academy of Sciences, Dalian 116023, China*

Corresponding authors: yuzj@qibebt.ac.cn(Zongjiang Yu); xuchao@qibebt.ac.cn(Chao Xu)

Content

Pages:37

Figures:45

Tables:3

Text S1. Experimental reagents

Pyrrole (99%, Anhui Senrise Technologies Co., Ltd.), para-methylbenzaldehyde (98%, Anhui Senrise Technologies Co., Ltd.), para-nitrobenzaldehyde (98%, Anhui Senrise Technologies Co., Ltd.), o-hydroxybenzaldehyde (AR, Anhui Senrise Technologies Co., Ltd.), propionic acid (≥99%, Anhui Senrise Technologies Co., Ltd.), anhydrous potassium carbonate (K_2CO_3, AR, Sinopharm Chemical Reagent Co., Ltd.), imidazole (AR, Sinopharm Chemical Reagent Co., Ltd.), stannous chloride dihydrate ($SnCl_2 \cdot 4H_2O$, 99%, Bide Pharmatech Co., Ltd.), ferrous chloride tetrahydrate ($FeCl_2 \cdot 4H_2O$, 98%, Shanghai Macklin Biochemical Co.,Ltd.), graphite powder (325 mesh, Meryer(Shanghai)Chemical Technology Co.,Ltd.), hydrogen peroxide (H_2O_2, AR, Sinopharm Chemical Reagent Co., Ltd.), concentrated hydrochloric acid (HCl, AR, Sinopharm Chemical Reagent Co., Ltd.), concentrated sulfuric acid (H_2SO_4, AR, Sinopharm Chemical Reagent Co., Ltd.), potassium permanganate ($KMnO_4$, AR, Sinopharm Chemical Reagent Co., Ltd.), 1-hydroxybenzotriazole (≥97%, Shanghai Macklin Biochemical Co.,Ltd.), and cyclohexylcarbodiimide (98%, Anhui Senrise Technologies Co., Ltd.) were used directly in the synthesis experiment without further purification.

Text S2. Supplementary characterization methods

LC-MS detection method: The novel porphyrin intermediate was dissolved in dichloromethane. About 1 mL of the solution was placed in a sample bottle. The mass spectrometer (3000UHPLC-QT 0203 G003, Bruker) was used for determination. The mobile phase was prepared by mixing water (0.1 % formic acid) and acetonitrile (0.1 % formic acid) in a 1:1 ratio. The flow rate was set to 0.2 $mL \cdot min^{-1}$, the column temperature was maintained at 40 °C, and the ultraviolet detector wavelength was 278 nm. The m/z range was 50–1500.

^{1}H NMR detection method: After the new porphyrin sample is fully dried, an appropriate amount of sample is added to an NMR tube, followed by an appropriate amount of deuterated reagent to fully dissolve it. The ^{1}H NMR spectra were determined using a nuclear magnetic resonance spectrometer (AVANCE-III 600 MHz, Bruker BioSpin International AG), with the spectra processed using MestReNova software.

FT-IR detection method: Dry samples of new porphyrins and new iron porphyrins were mixed with KBr powder to prepare the samples. A total of 128 scans were acquired using a Thermo Fisher Nicolet 6700 FTIR spectrometer in the wavenumber range of 400 to 4000 cm^{-1}. The resulting spectra were smoothed and baseline-corrected by the software and then plotted using Origin software.

XPS detection method: The quantitative sample was placed on a tin foil, which was then fully compacted. The tin foil with the sample was mounted on the sample stage and analyzed using an X-ray Photoelectron Spectrometer (XPS, Shimadzu Corporation, Japan). The acquired spectrum was processed using XPSPEAK software. A binding energy of 284.8 eV for C 1s was used as the reference, and the valence state of iron (Fe) was determined. Finally, the results were plotted using Origin software.

Powder X-ray diffraction (XRD) was conducted at a scanning speed of 8° per minute, from 5° to 80°, with a step size of 0.02°, using an X-ray diffractometer (MiniFlex 600) at 36 kV and 30 mA.

SEM Detection Method: Conductive adhesive containing the sample was attached to the sample stage and coated with a thin layer of gold to enhance conductivity. Subsequently, the microscopic morphology of the immobilized materials was examined using cold field emission scanning electron microscopy (SEM, Hitachi S-4800, Japan).

The uniformity of the elemental distribution was analyzed via energy-dispersive X-ray spectroscopy (EDS).

The thermogravimetric curve of ferroporphyrin was determined using a simultaneous thermogravimetry-differential scanning calorimeter (STA 449 F5 Jupiter). After weighing the crucible, an appropriate amount of the sample was placed into the crucible, and the measurement program was initiated. The analysis was performed under nitrogen atmosphere with a flow rate of 20 mL/min, a temperature range of 30°C to 600°C, and a heating rate of 10°C/min.

The Elementar UNICUBE elemental analyzer was used to determine the C, H, and N contents of ferroporphyrin samples, which verified the molecular composition, stoichiometric ratio, metal coordination structure integrity, and sample purity.

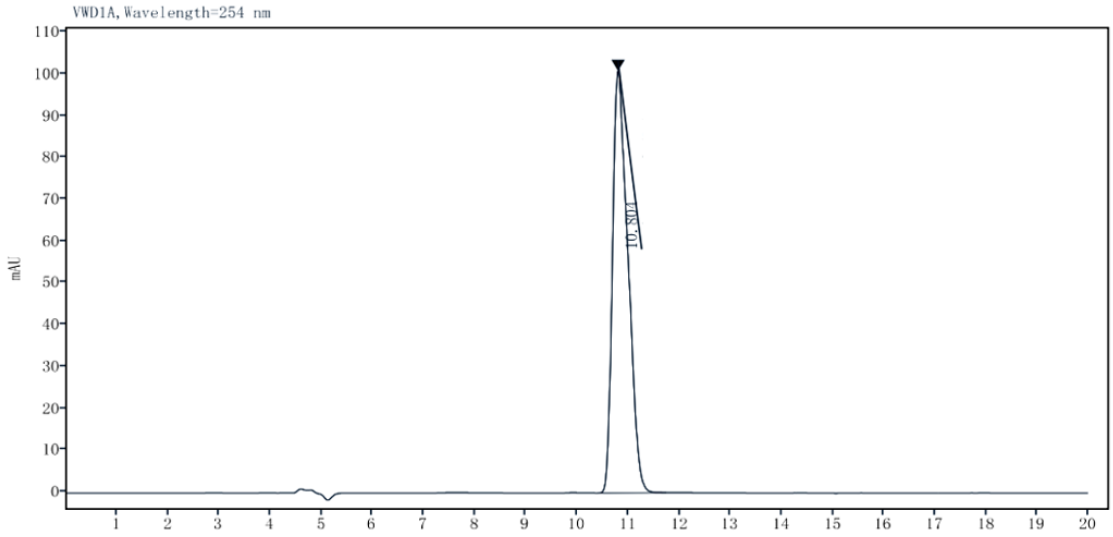

Figure S1. Liquid chromatogram of 4-bromo-2,6-difluoroaniline

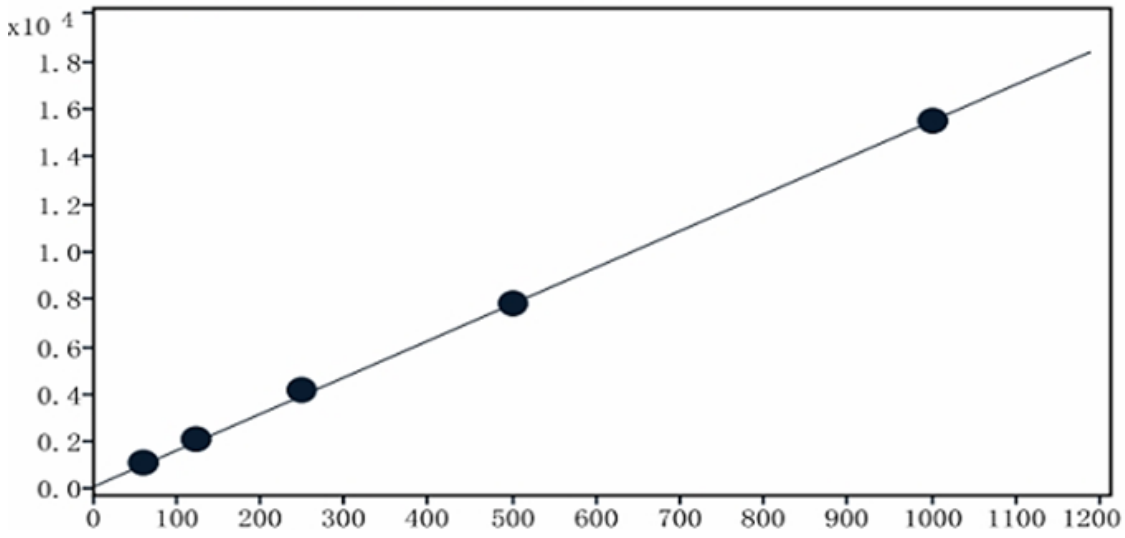

Figure S2. Standard curve equation for 4-bromo-2,6-difluorobenzene

Note: The retention time of 4-bromo-2,6-difluoroaniline is 10.79 minutes. The standard curve equation was obtained via linear regression analysis, yielding the regression equation: Y = 15.4141X + 159.6783. In this equation: Y represents the peak area. X represents the concentration of 4-bromo-2,6-difluoroaniline (ppm).

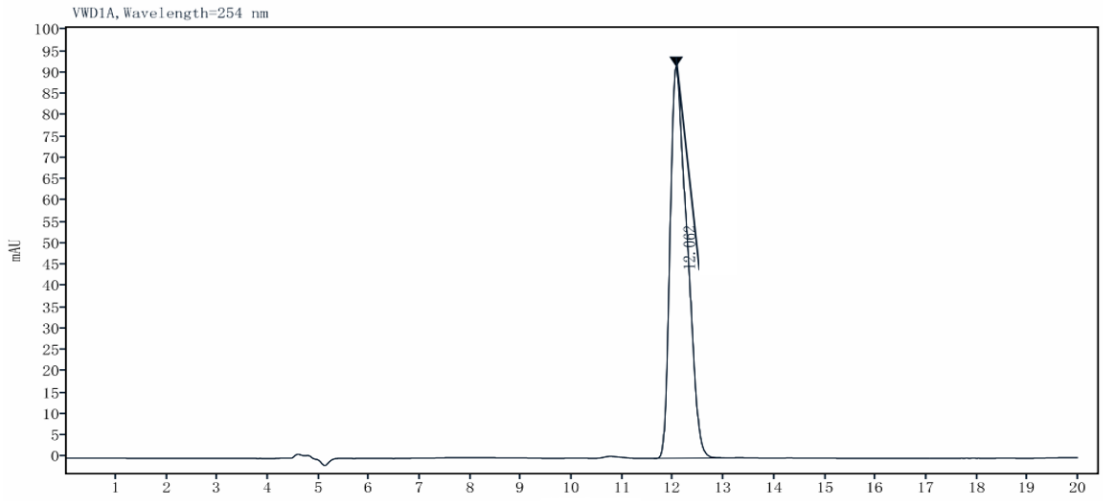

Figure S3. Liquid chromatogram of 5-bromo-1,3-difluoro-2-nitrobenzene

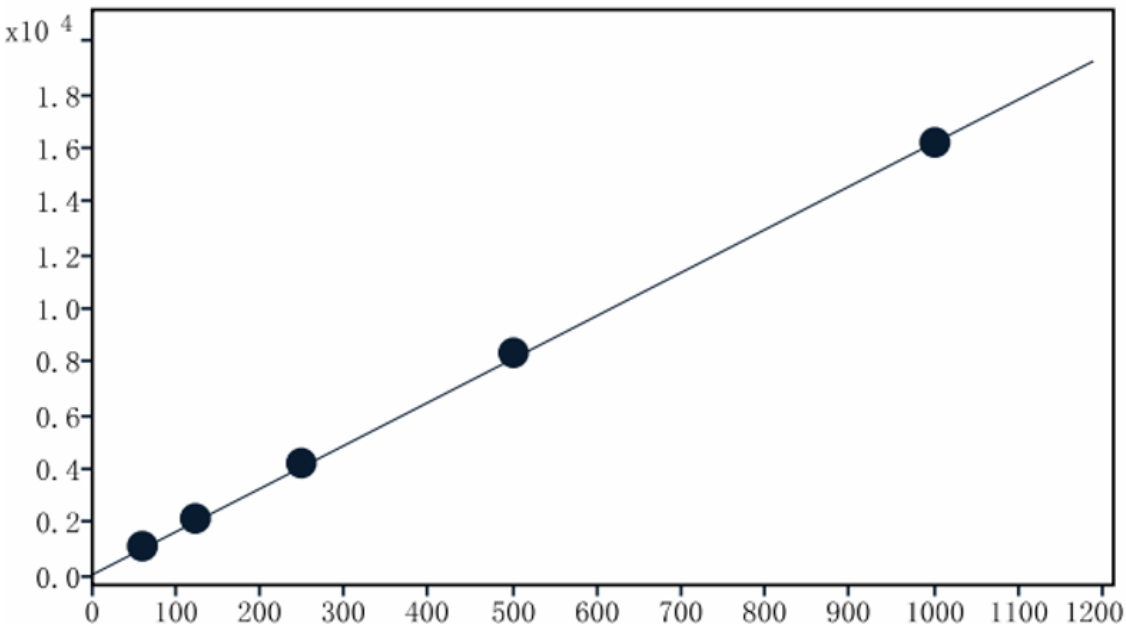

Figure S4. Standard curve equation for 5-bromo-1,3-difluoro-2-nitrobenzene

Note: The retention time of 5-bromo-1,3-difluoro-2-nitrobenzene is 12.07 minutes. The standard curve equation was obtained via linear regression analysis, yielding the regression equation: Y=16.1711X+90.5742. In this equation: Y represents the peak area. X represents the concentration of 5-bromo-1,3-difluoro-2-nitrobenzene (ppm).

Table S1. Screening of iron porphyrin substituents

Entry	catalys	oxidant	Conversion(%)	Yield(%)
1	FeTPP（-H）	TBHP	39.00%	9.76%
2	FeTMOPP（-OCH_3）	TBHP	71.23%	19.08%
3	FeTFMPP（-CF_3）	TBHP	59.46%	5.71%
5	FeTBPP（-Br）	TBHP	47.61%	12.46%
6	FeTFOPP（-OCF_3）	TBHP	39.00%	9.31%
7	FeTMPP（-CH_3）	TBHP	43.93%	20.86%
8	FeTAPP（-NH_2）	TBHP	41.21%	18.64%

The reaction conditions are as follows: 4-bromo-2,6-difluoroaniline (0.25 mmol, 50 mg); iron porphyrin(1.25×10^{-6}mol); tert-butyl hydrogen peroxide (0.75mmol, 103 μL); methylene chloride (10 mL); temperature (room temperature); time varied, with

entry 8 requiring 24 hours, while others required 4 hours.

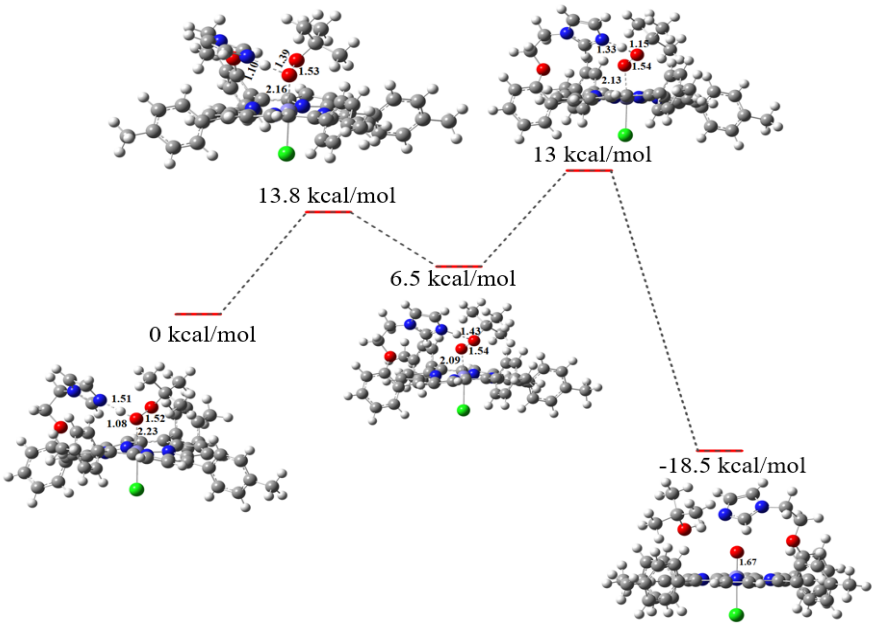

Figure S5. The process by which FeC_2IPP interacts with TBHP to generate Fe $^{IV+\bullet}$=O

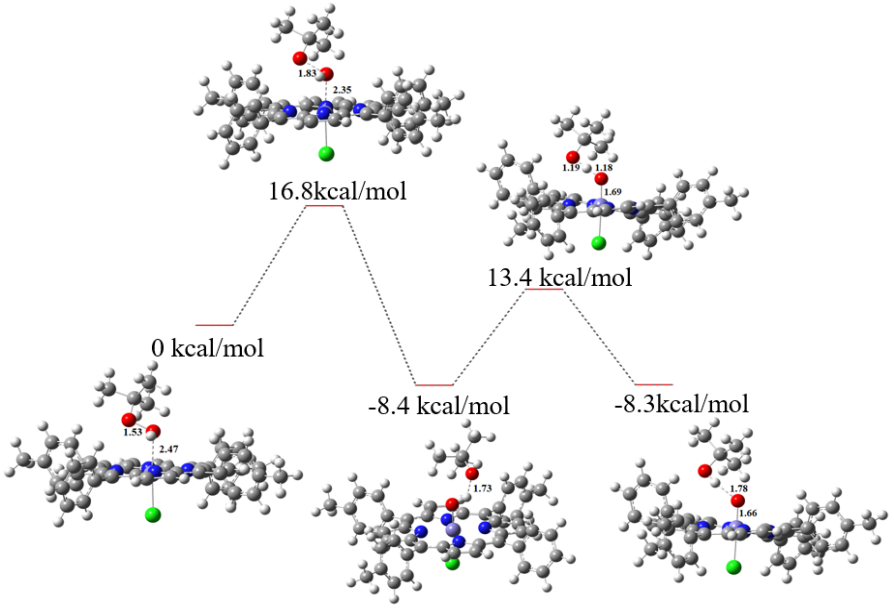

Figure S6. The process by which FeTMPP interacts with TBHP to generate Fe $^{IV+\bullet}$=O

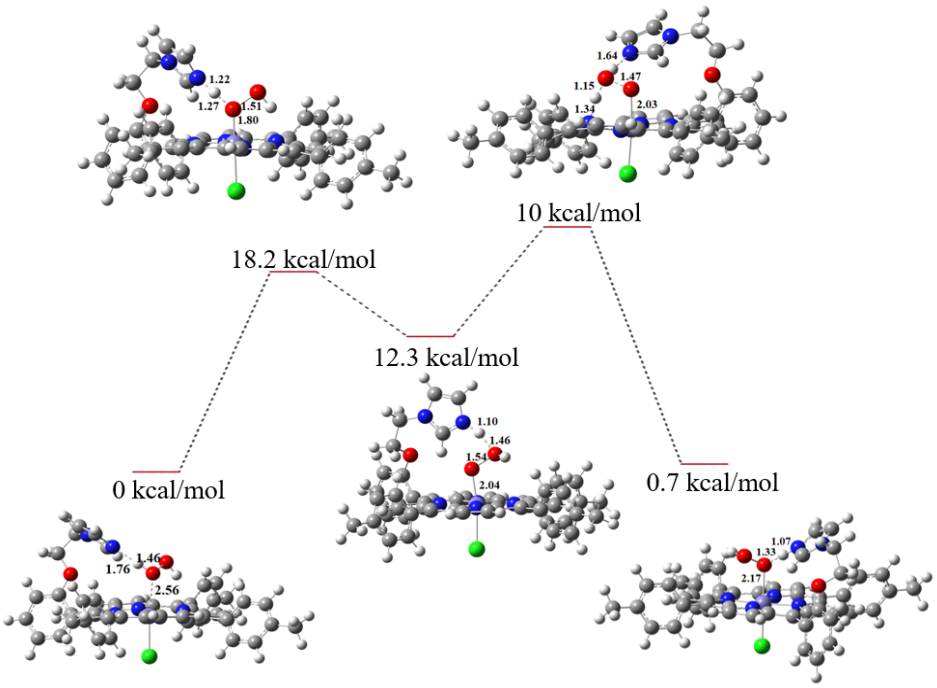

Figure S7. The process by which FeC_2IPP interacts with H_2O_2 to generate $Fe^{IV+\bullet}=O$

Text S3. Synthesis method of FeC_nIPP

Synthesis of Compound A [1, 2]: First, o-hydroxybenzaldehyde (0.02 mol) was dissolved in 300 mL of propionic acid, followed by the addition of p-methylbenzaldehyde (0.06 mol). The mixture was stirred to ensure complete dissolution. After heating the temperature to 141°C, the new distilled pyrrole (0.08 mol) was slowly added dropwise over a period of approximately 20 minutes. With the addition of pyrrole, the color of the solution gradually changed to brownish-black. The reaction temperature was maintained at 131°C for 0.5 hours. After the reaction was complete, the mixture was cooled and allowed to stand for a period of time, during which a purple solid precipitated. The solids were collected by filtration, washed with absolute ethanol until a light purple color was achieved, and then air-dried to obtain the crude product. Finally, the target product was purified using column chromatography.

Synthesis of Compounds B1–B5 [3]: Compound A (0.075 mmol) was dissolved in 5 mL of N,N-dimethylformamide (DMF) and refluxed until dissolved. Bromoalkanes

(1.12 mmol), roasted anhydrous potassium carbonate (1.12 mmol), were added, and the mixture was stirred at room temperature for 48 hours. Thin-layer chromatography (TLC) was used to monitor the reaction progress until it was nearly complete. The reaction mixture was then poured into ice-cold water containing 10% methanol. A purple flocculent precipitate was obtained, which was filtered, washed with methanol to remove any residual bromoalkanes and DMF, and air-dried to yield the crude product. The final products, B1–B5, were obtained by purification using column chromatography.

Synthesis of compounds C1-C5[4]: Compounds B1–B5 (0.063 mmol each) and imidazole (2.51 mmol) were dissolved in 10 mL of dimethylformamide (DMF), and potassium carbonate (2.51 mmol) was then added. After stirring the mixture at room temperature in the dark, no raw materials remained, indicating the reaction was complete. The anhydrous potassium carbonate was removed by filtration, and the DMF was spun dry to obtain the crude products. The target products, C1–C5, were successfully obtained by column chromatography.

Synthesis of compounds D1-D5 [5]: Compounds C1–C5 (each 0.063 mmol) and $FeCl_2 \cdot 4H_2O$ (2.51 mmol) were dissolved in 10 mL of dimethylformamide (DMF). After heating the reaction mixture at 120°C for 2 hours, it was cooled to room temperature. The metal salts were removed by filtration, and the DMF was spun dry. A mixture of dichloromethane (DCM) and water was used to extract the organic phase. The DCM phase was collected, and the crude product was obtained after spin-drying. Finally, the target products D1–D5 were purified via column chromatography.

Text S4. Synthesis method of $FeTAC_2IPP$

Synthesis of compound E [6]: o-hydroxybenzaldehyde (0.02 mol) and p-

nitrobenzaldehyde (0.06 mol) were added to refluxing propionic acid (300 mL), and after the aldehyde was completely dissolved, the newly distilled pyrrole (0.08 mol) was slowly added dropwise over 20 minutes and refluxed for 1 hour. Upon cooling of the reaction mixture, it was left to stand overnight. The mixture was then diluted with distilled water (1 L), and the pH was adjusted to 6–7 using a 6 mol/L sodium hydroxide solution. It was filtered, washed five times with hot water, and the resulting black-purple powder mixture was dried overnight in an 80°C vacuum oven to obtain a crude product. The crude product was then subjected to column chromatography to obtain the target product E.

Synthesis of compound F: Compound E (0.57 mmol) was dissolved in 50 mL of dimethylformamide (DMF) and refluxed to ensure complete dissolution. Subsequently, 1,2-dibromoethane (9.75 mmol) and roasted anhydrous potassium carbonate (9.75 mmol) were added to the solution. The mixture was stirred at room temperature for 48 hours, and the progress of the reaction was monitored using thin-layer chromatography (TLC) until the reaction was nearly complete. The reaction mixture was then poured into ice-cold water containing 10% methanol, resulting in the precipitation of a flocculent purple precipitate. The precipitate was filtered, washed with methanol to remove any residual 1,2-dibromoethane and DMF, and dried to obtain the crude product. Finally, the crude product was purified via column chromatography to yield the target product F.

Synthesis of compound G: Compound F (0.057 mmol) and imidazole (2.77 mmol) were dissolved in 10 mL of dimethylformamide (DMF). Following this, potassium carbonate (2.77 mmol) was added to the solution. The mixture was stirred at room temperature in the dark for a sufficient period to ensure that no residual raw materials

remained. After completing the reaction, the anhydrous potassium carbonate was removed by filtration. The DMF was then spun dry to obtain the crude product. Finally, the crude product was purified via column chromatography to yield the target product G.

Synthesis of compound H [7]: Compound G (0.027 mmol) was dissolved in concentrated hydrochloric acid (36%, 20 mL) at room temperature. Excess stannous chloride ($SnCl_2 \cdot 2H_2O$, 0.44 mmol) was added to the solution. The resulting green mixture was cautiously heated to 65–70 °C and maintained at that temperature for 30 minutes. Subsequently, the mixture was neutralized with concentrated ammonia water under ice bath conditions and filtered. The filter cake was repeatedly extracted with dichloromethane (DCM). The extracted solution was concentrated under reduced pressure to obtain a crude product. Finally, the crude product was purified via column chromatography to yield the target product H.

Synthesis of compound I: Compound D (0.026 mmol) and ferrous chloride tetrahydrate (1.00 mmol) were dissolved in 25 mL of dimethylformamide (DMF), and the solution was subjected to a reaction at 120 °C for 2 hours. Upon cooling to room temperature, the ferrous chloride tetrahydrate residue was removed by filtration. The DMF was then spun dry to isolate the solid, which was subsequently dissolved in 1 mol/L hydrochloric acid (HCl). Ammonium hydroxide ($NH_3 \cdot H_2O$) was added to precipitate the solid, which was then filtered, washed with distilled water, and vacuum dried at 60 °C for 24 hours to obtain the crude product. Finally, the purified product $FeTAC_2IPP$ was obtained through column chromatography.

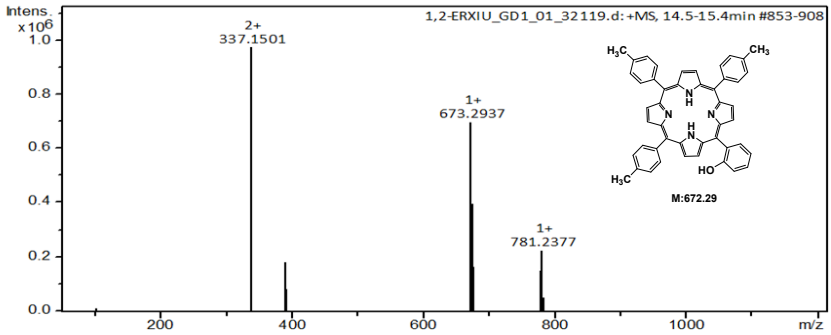

Figure S8. Liquid mass spectrum of compound A

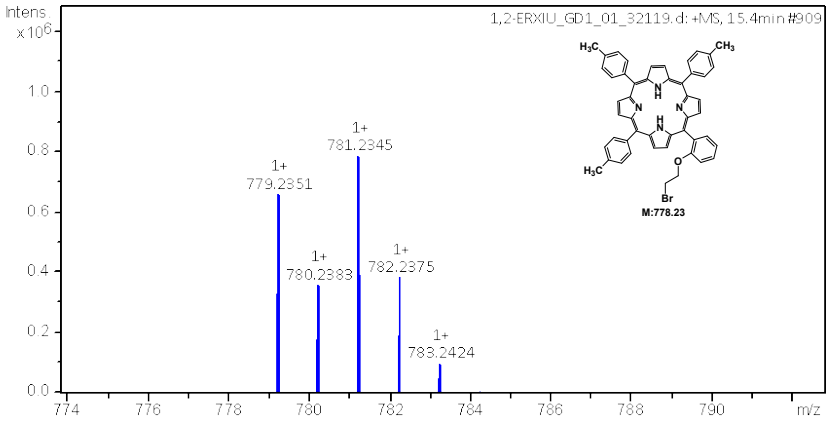

Figure S9. Liquid mass spectrum of compound B1

Notes: Compound B1: HRMS (ESI): m/z 779.2351 ([M+H]$^+$), 781.2345 ([M+2+H]$^+$)

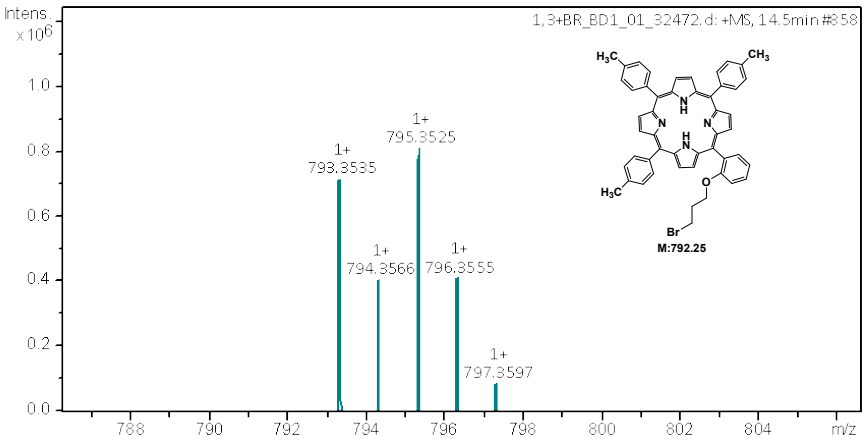

Figure S10. Liquid mass spectrum of compound B2

Notes: Compound B2: HRMS (ESI): m/z 793.3535 ([M+H]$^+$), 795.3525 ([M+2+H]$^+$)

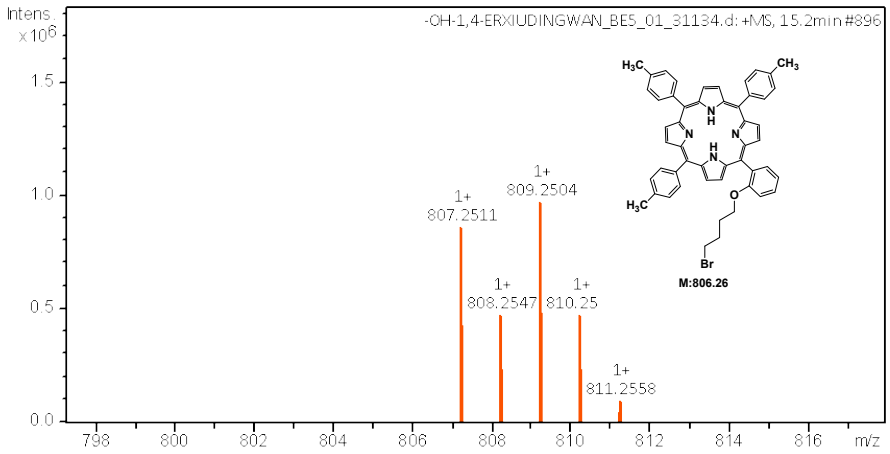

Figure S11. Liquid mass spectrum of compound B3

Notes: Compound B3: HRMS (ESI): m/z 807.2511 ([M+H]$^+$), 809.2504 ([M+2+H]$^+$)

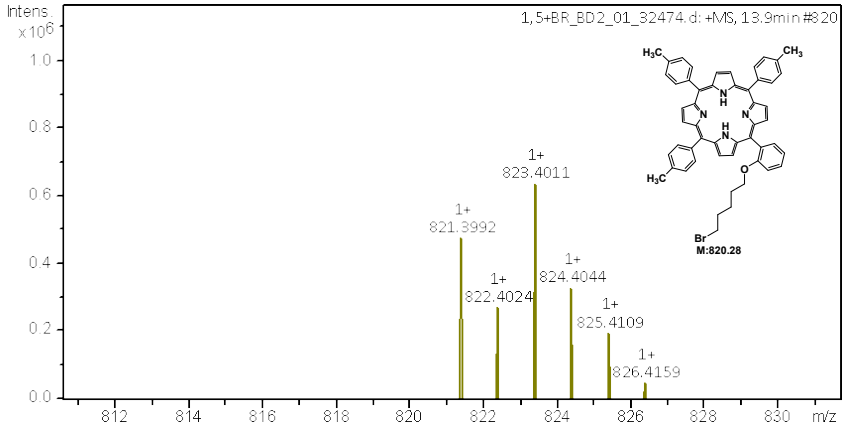

Figure S12. Liquid mass spectrum of compound B4

Notes: Compound B4: HRMS (ESI): m/z 821.3992 ([M+H]$^+$), 823.4011 ([M+2+H]$^+$)

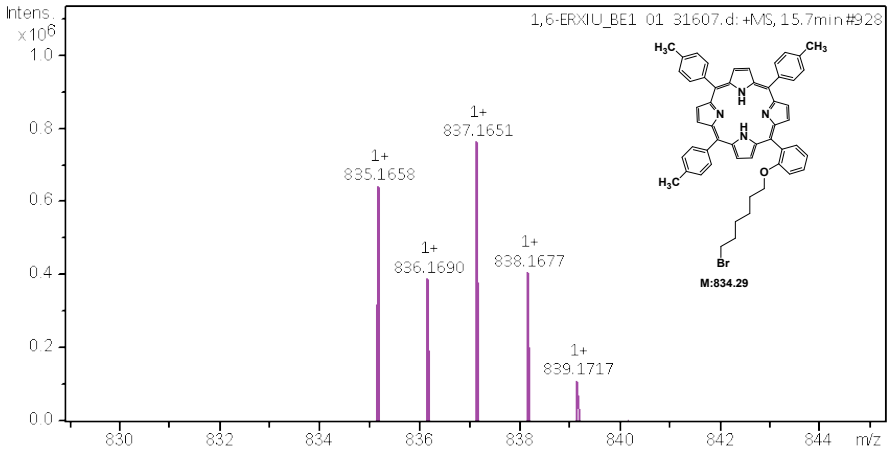

Figure S13. Liquid mass spectrum of compound B5

Notes: Compound B5: HRMS (ESI): m/z 835.1658 ([M+H]$^+$), 837.1651 ([M+2+H]$^+$)

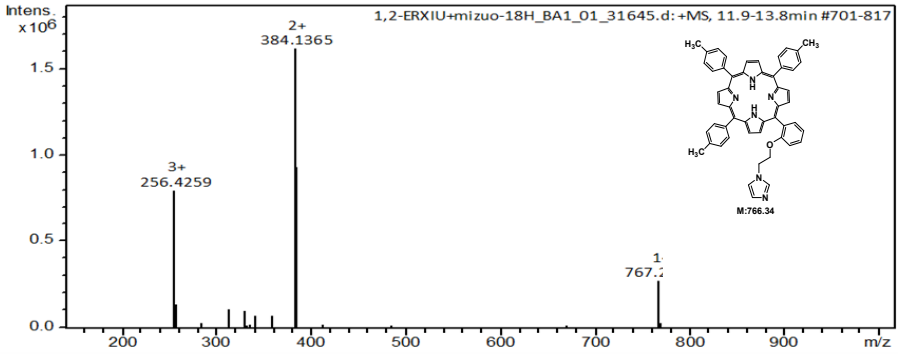

Figure S14. Liquid mass spectrum of compound C1

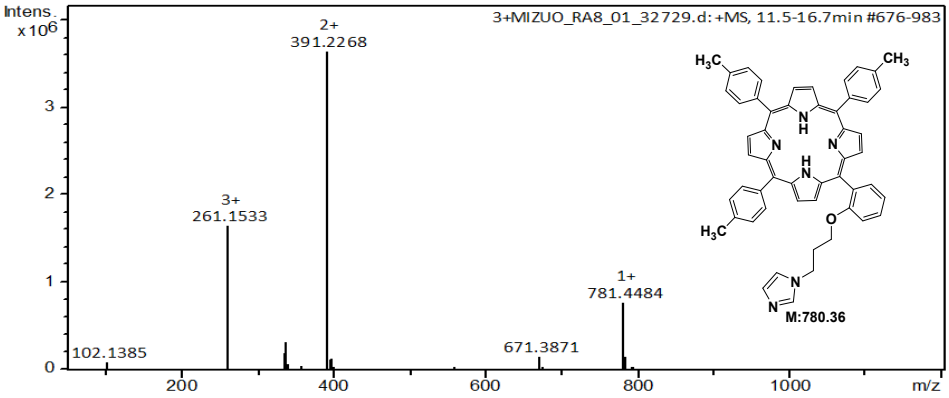

Figure S15. Liquid mass spectrum of compound C2

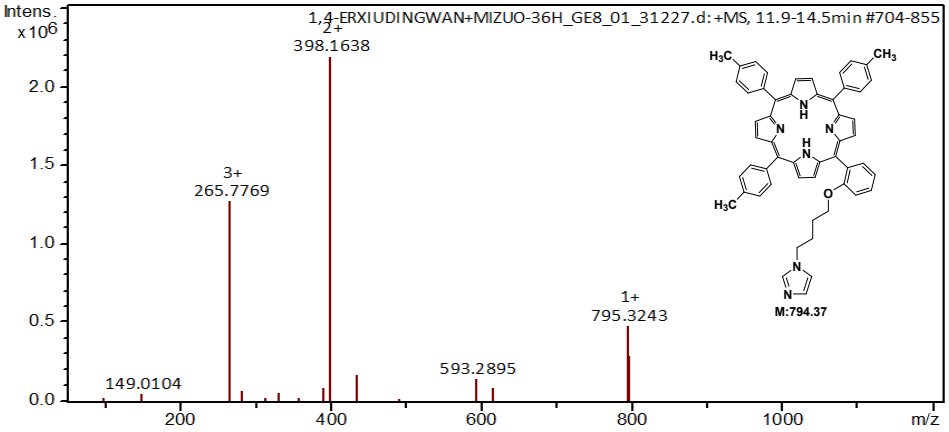

Figure S16. Liquid mass spectrum of compound C3

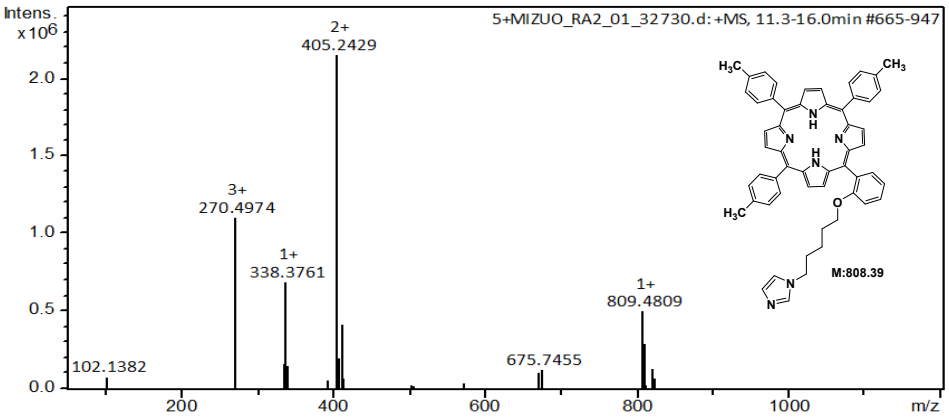

Figure S17. Liquid mass spectrum of compound C4

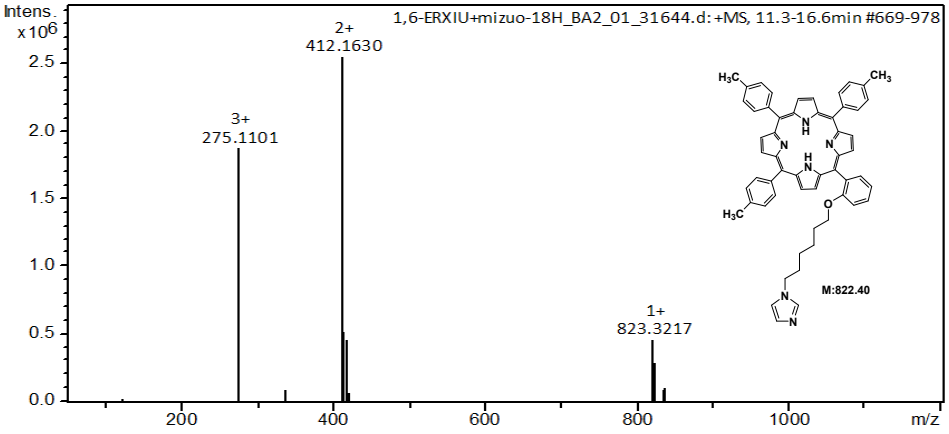

Figure S18. Liquid mass spectrum of compound C5

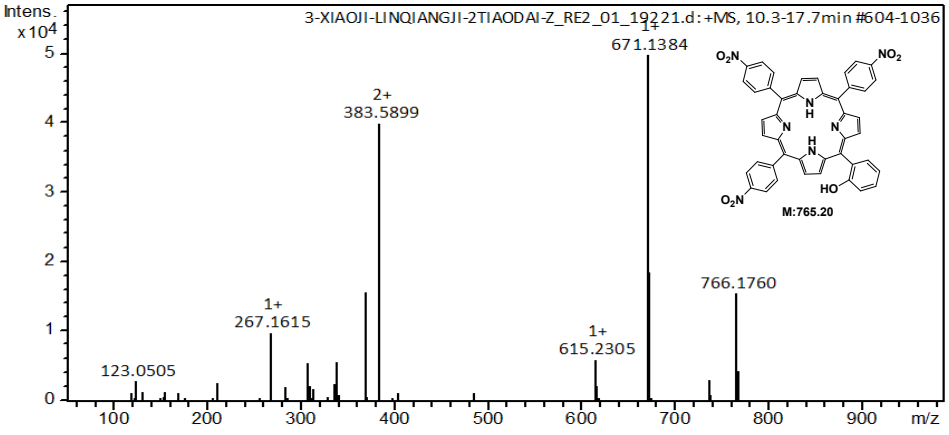

Figure S19. Liquid mass spectrum of compound E

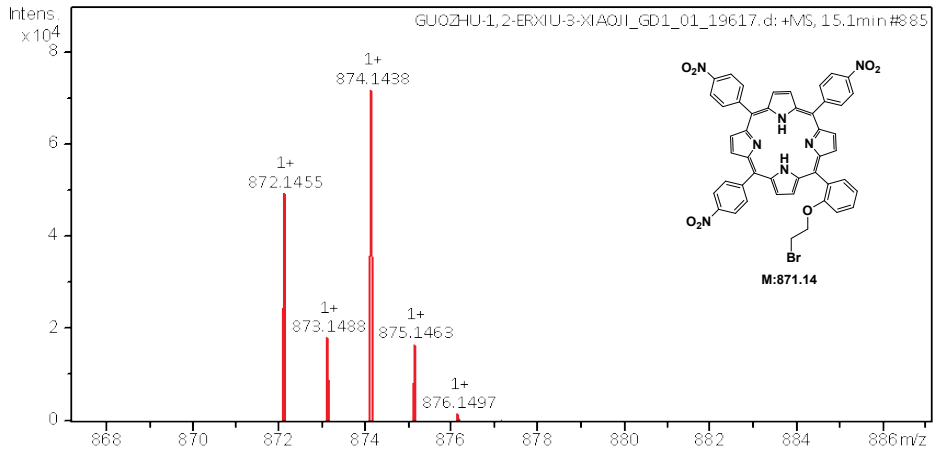

Figure S20. Liquid mass spectrum of compound F

Notes: Compound F: HRMS (ESI): m/z 872.1455 ([M+H]$^+$), 874.1438 ([M+2+H]$^+$)

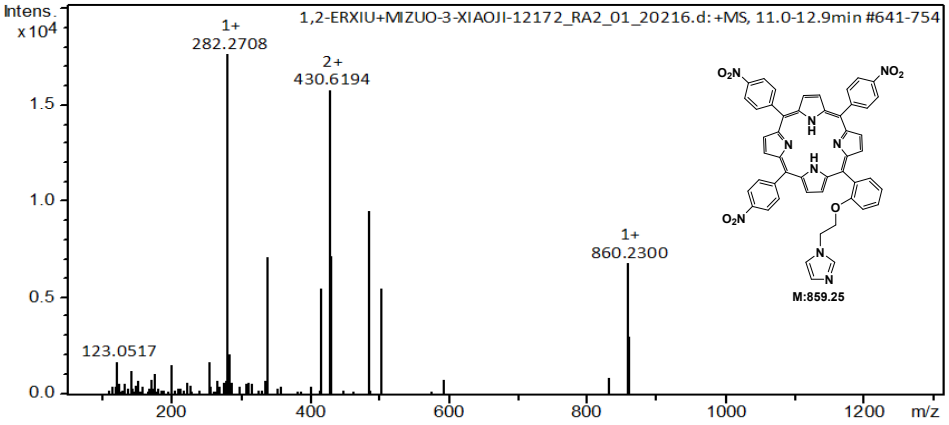

Figure S21. Liquid mass spectrum of compound G

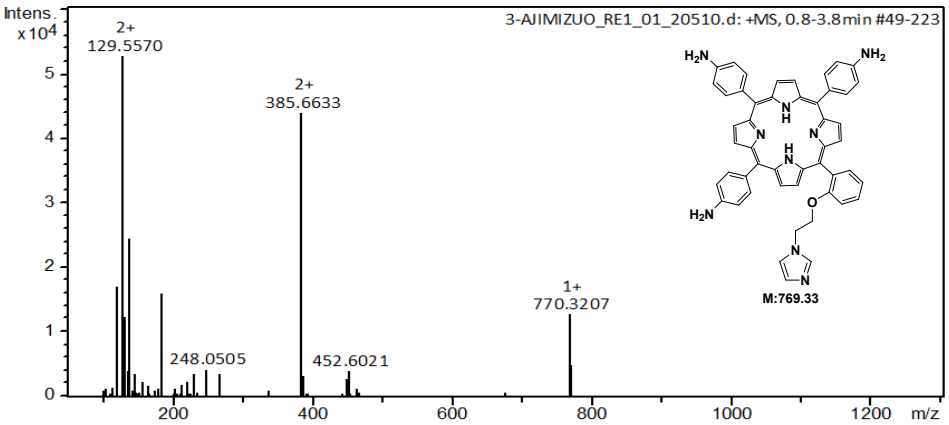

Figure S22. Liquid mass spectrum of compound H

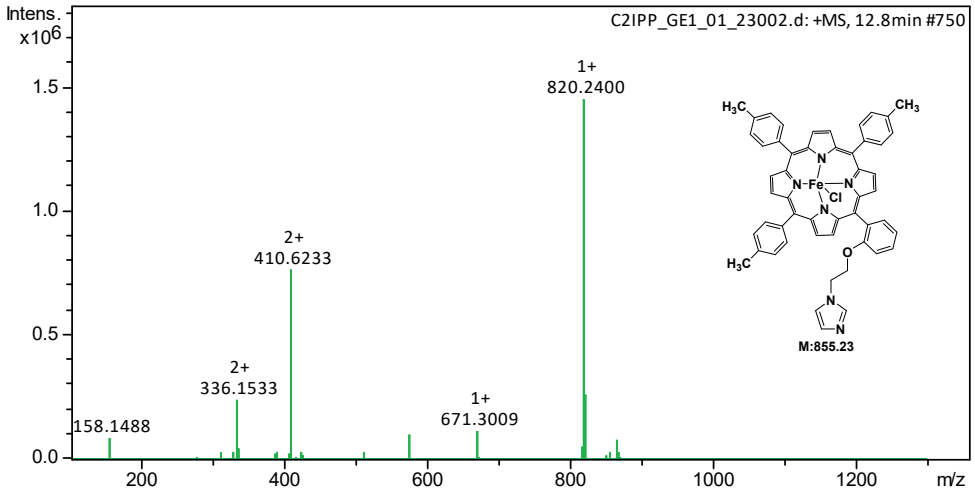

Figure S23. Liquid mass spectrum of compound D1

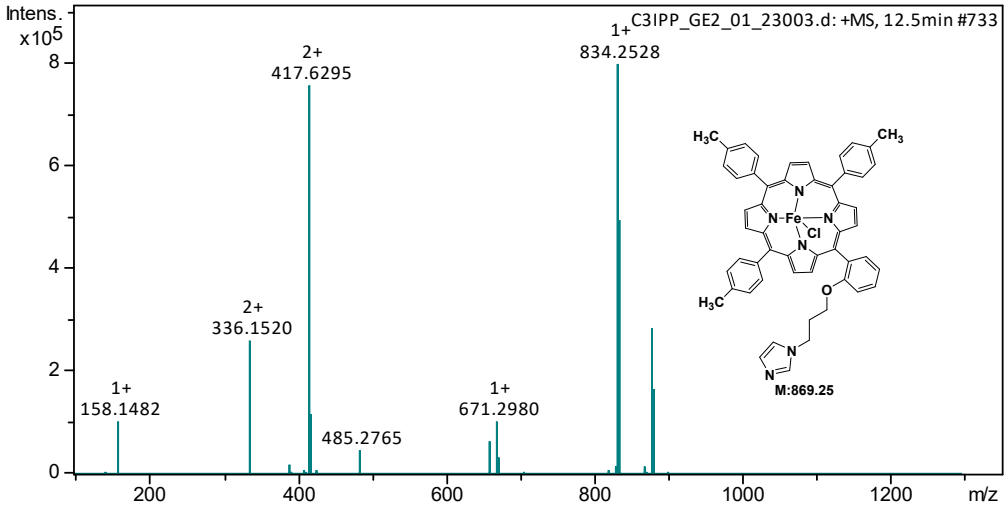

Figure S24. Liquid mass spectrum of compound D2

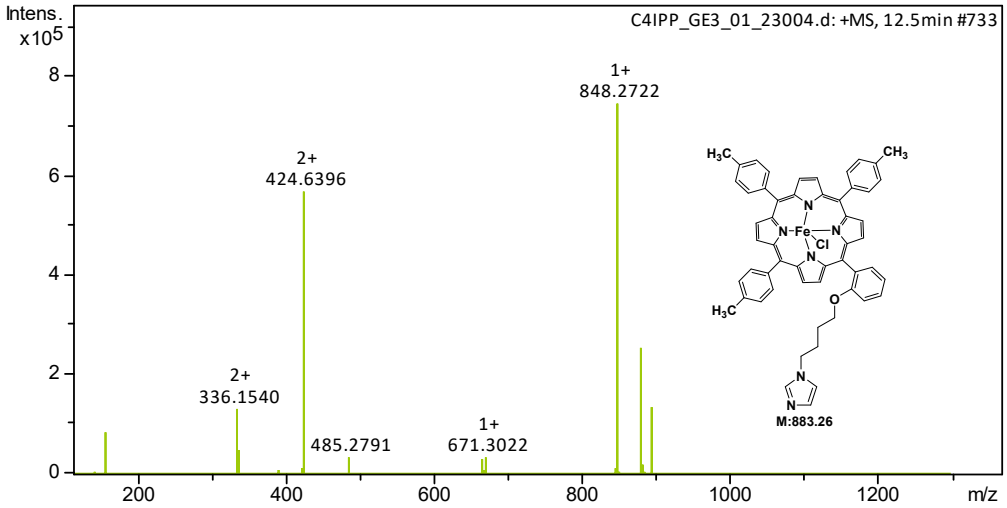

Figure S25. Liquid mass spectrum of compound D3

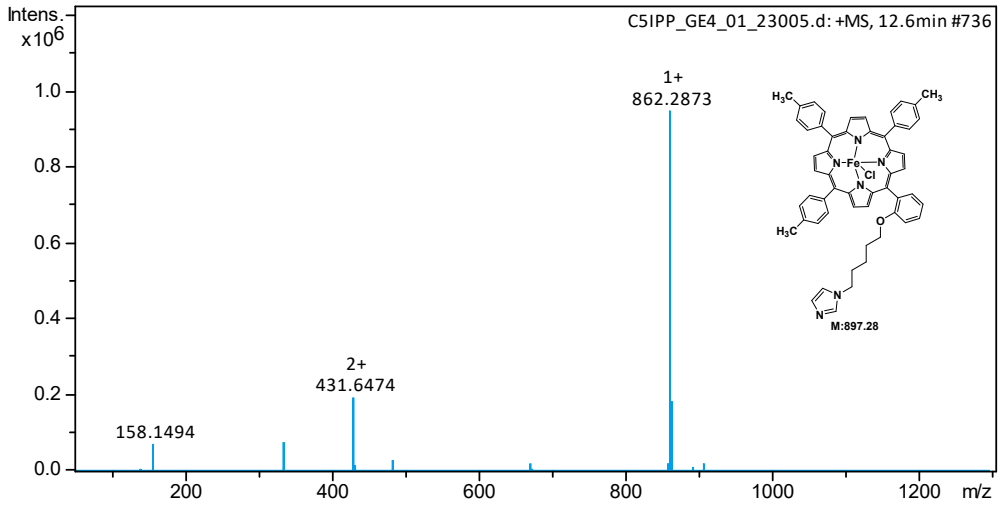

Figure S26. Liquid mass spectrum of compound D4

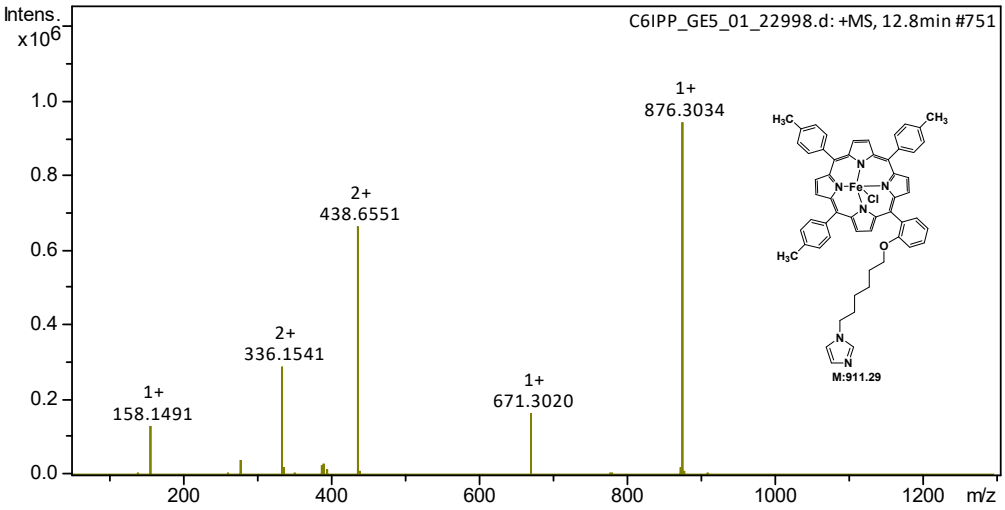

Figure S27. Liquid mass spectrum of compound D5

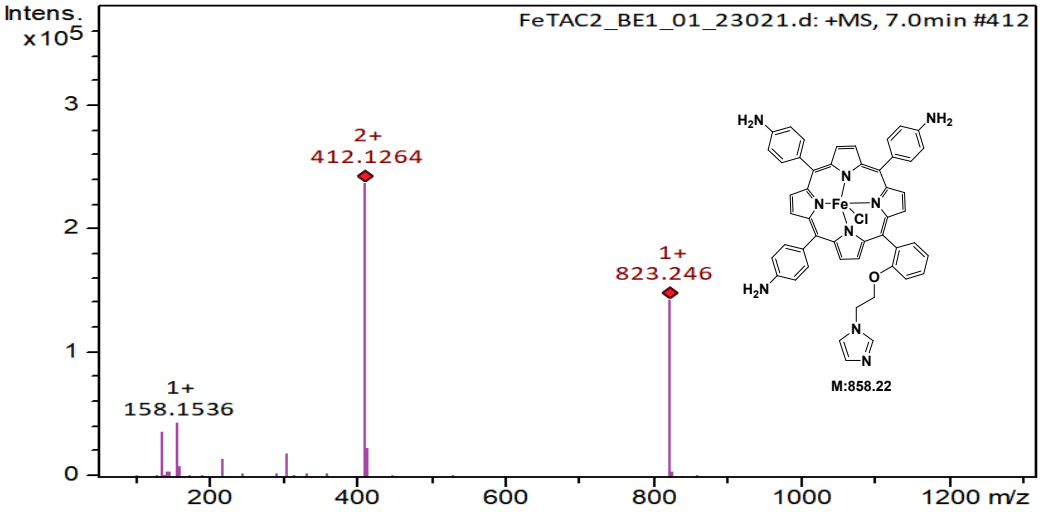

Figure S28. Liquid mass spectrum of compound I

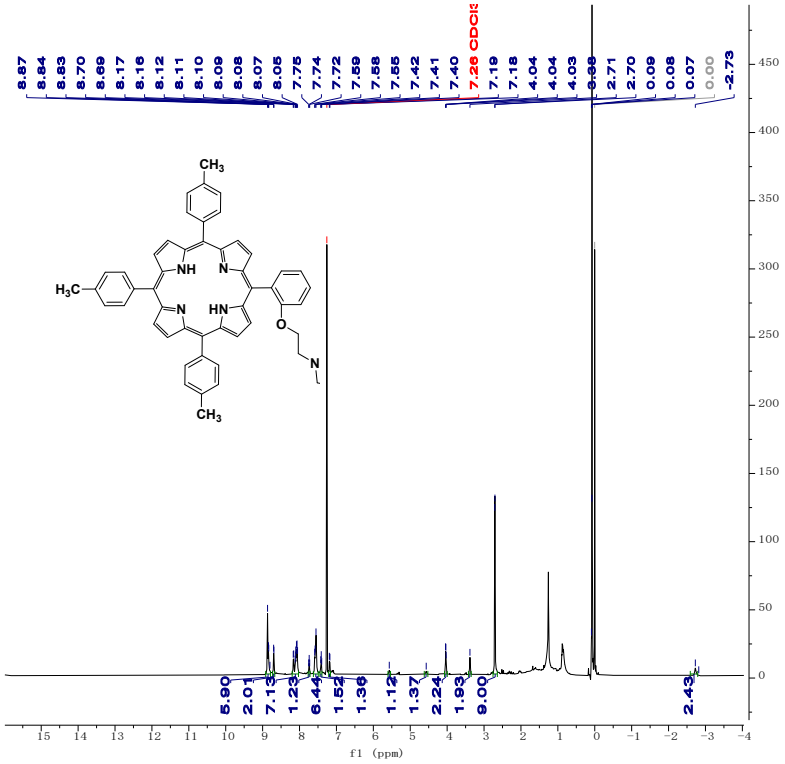

Parameter	
1	Jan09-2024-csj-1,2-mizuo.1.fid
2 Comment	
3 Origin	Bruker BioSpin GmbH
4 Owner	nmr600
5 Site	
6 Instrument	spect
7 Solvent	CDCl3
8 Temperature	298.0
9 Pulse Sequence	zg30
10 Experiment	1D
11 Probe	5 mm CPTCI 1H-13C/15N/ D Z-GRD Z75812/0058
12 Number of Scans	8
13 Receiver Gain	20.2
14 Relaxation Delay	1.0000
15 Pulse Width	7.0500
16 Presaturation Frequency	
17 Acquisition Time	1.3631
18 Acquisition Date	2024-01-09T09:04:00
19 Modification Date	2024-06-26T15:41:45
20 Spectrometer Frequency	600.13
21 Spectral Width	12019.2
22 Lowest Frequency	-2426.2
23 Nucleus	1H
24 Acquired Size	16384
25 Spectral Size	131072
26 Digital Resolution	0.09

Figure S29. NMR spectrum of C_2IPP

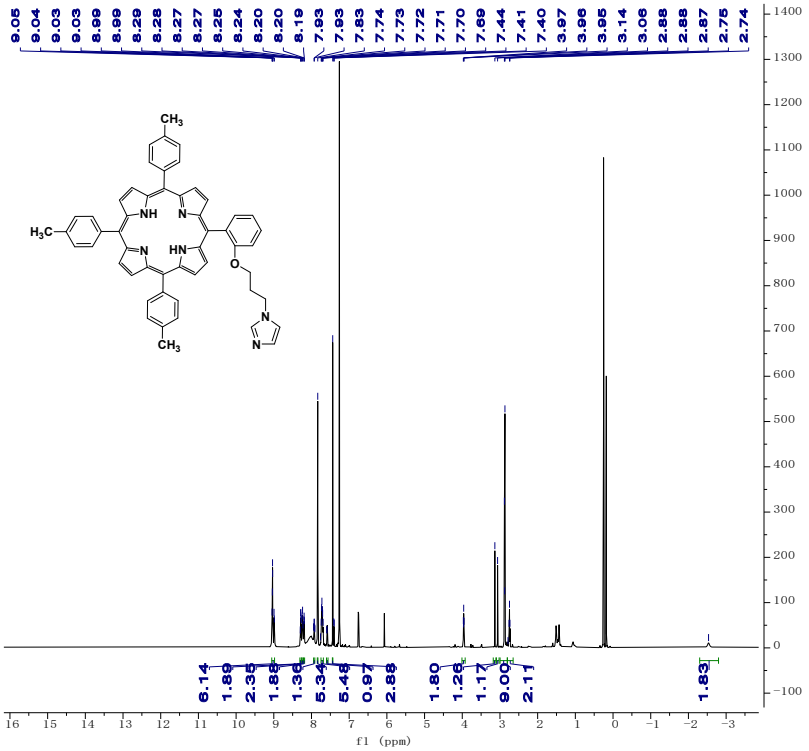

Parameter	
1	Feb29-2024-3+mizuo-cdc13.1.fid
2 Comment	
3 Origin	Bruker BioSpin GmbH
4 Owner	nmr600
5 Site	
6 Instrument	spect
7 Solvent	CDCl3
8 Temperature	298.0
9 Pulse Sequence	zg30
10 Experiment	1D
11 Probe	5 mm CPTCI 1H-13C/15N/ D Z-GRD Z75812/0058
12 Number of Scans	8
13 Receiver Gain	20.2
14 Relaxation Delay	1.0000
15 Pulse Width	7.0500
16 Presaturation Frequency	
17 Acquisition Time	1.3631
18 Acquisition Date	2024-02-29T11:14:00
19 Modification Date	2024-02-29T17:29:58
20 Spectrometer Frequency	600.13
21 Spectral Width	12019.2
22 Lowest Frequency	-2320.3
23 Nucleus	1H
24 Acquired Size	16384
25 Spectral Size	131072
26 Digital Resolution	0.09

Figure S30. NMR spectrum of C_3IPP

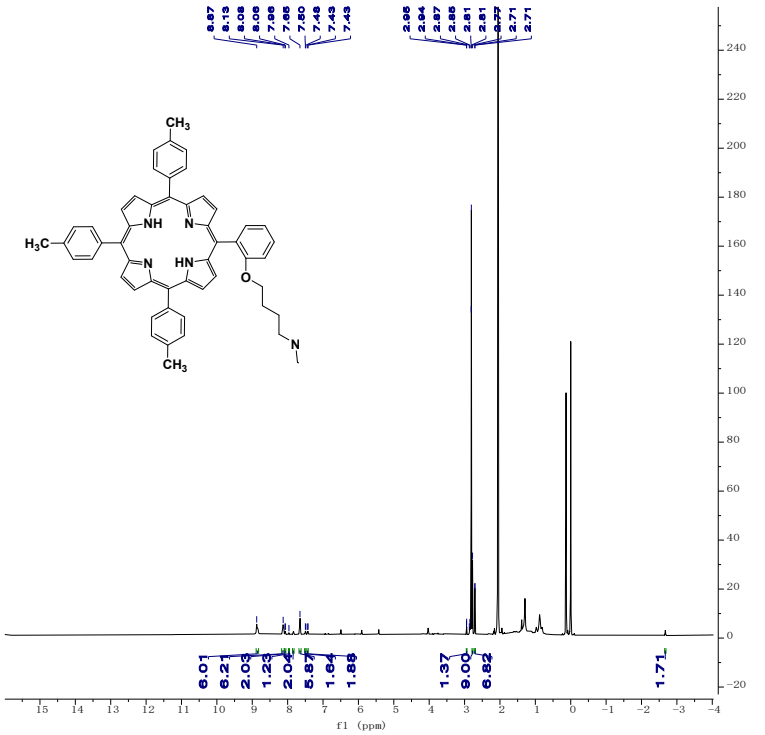

Parameter	
1	Dec15-2023-csj+mizuo.1.fid
2 Comment	
3 Origin	Bruker BioSpin GmbH
4 Owner	nmr600
5 Site	
6 Instrument	spect
7 Solvent	Acetone
8 Temperature	298.2
9 Pulse Sequence	zg30
10 Experiment	1D
11 Probe	5 mm CPTCI 1H-13C/15N/ D Z-GRD Z75812/0058
12 Number of Scans	8
13 Receiver Gain	20.2
14 Relaxation Delay	1.0000
15 Pulse Width	7.0500
16 Presaturation Frequency	
17 Acquisition Time	1.3631
18 Acquisition Date	2023-12-15T09:41:00
19 Modification Date	2023-12-15T16:55:25
20 Spectrometer Frequency	600.13
21 Spectral Width	12019.2
22 Lowest Frequency	-2421.5
23 Nucleus	1H
24 Acquired Size	16384
25 Spectral Size	131072
26 Digital Resolution	0.09

Figure S31. NMR spectrum of C_4IPP

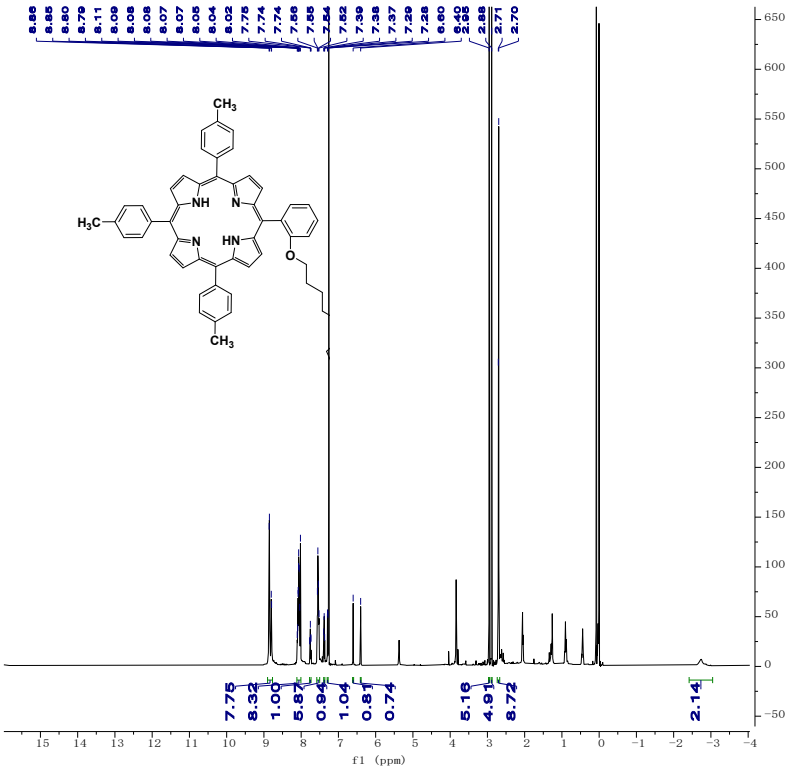

Parameter	
1	Feb29-2024-5+mizuo-cdcl3.1.fid
2 Comment	
3 Origin	Bruker BioSpin GmbH
4 Owner	nmr600
5 Site	
6 Instrument	spect
7 Solvent	CDCl3
8 Temperature	298.0
9 Pulse Sequence	zg30
10 Experiment	1D
11 Probe	5 mm CPTCI 1H-13C/15N/ D Z-GRD Z75812/0058
12 Number of Scans	8
13 Receiver Gain	20.2
14 Relaxation Delay	1.0000
15 Pulse Width	7.0500
16 Presaturation Frequency	
17 Acquisition Time	1.3631
18 Acquisition Date	2024-02-29T11:20:00
19 Modification Date	2024-02-29T16:38:47
20 Spectrometer Frequency	600.13
21 Spectral Width	12019.2
22 Lowest Frequency	-2428.1
23 Nucleus	1H
24 Acquired Size	16384
25 Spectral Size	131072
26 Digital Resolution	0.09

Figure S32. NMR spectrum of C_5IPP

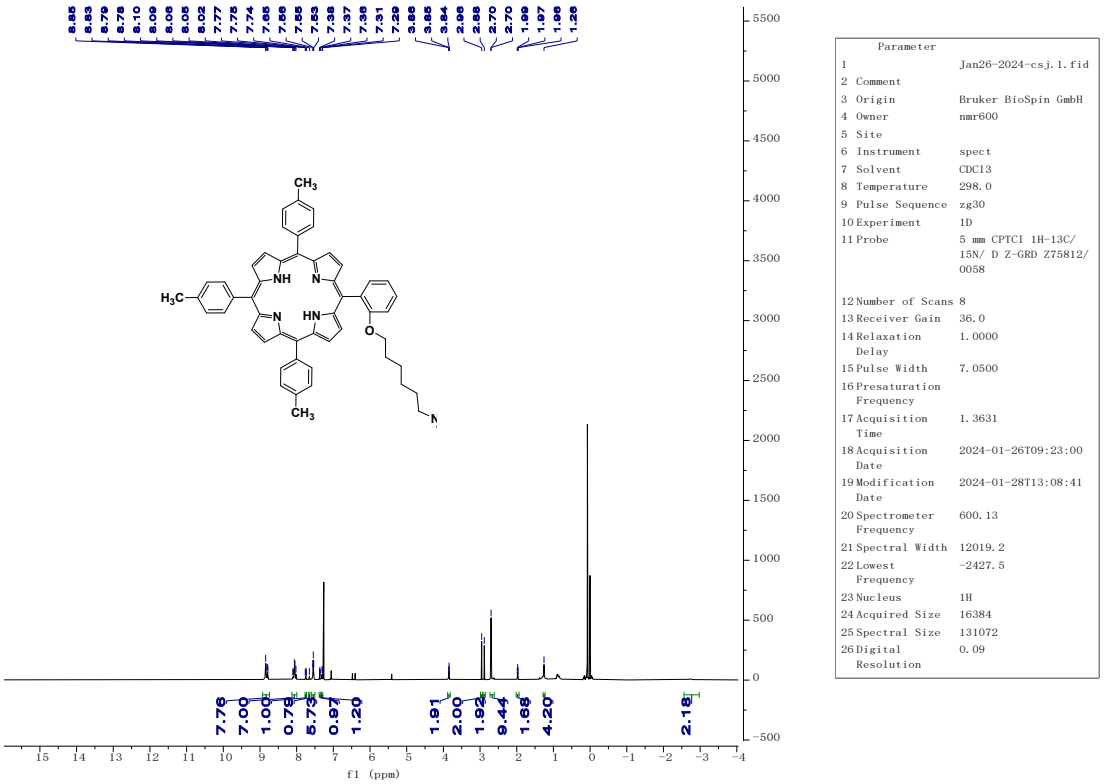

Figure S33. NMR spectrum of C_6IPP

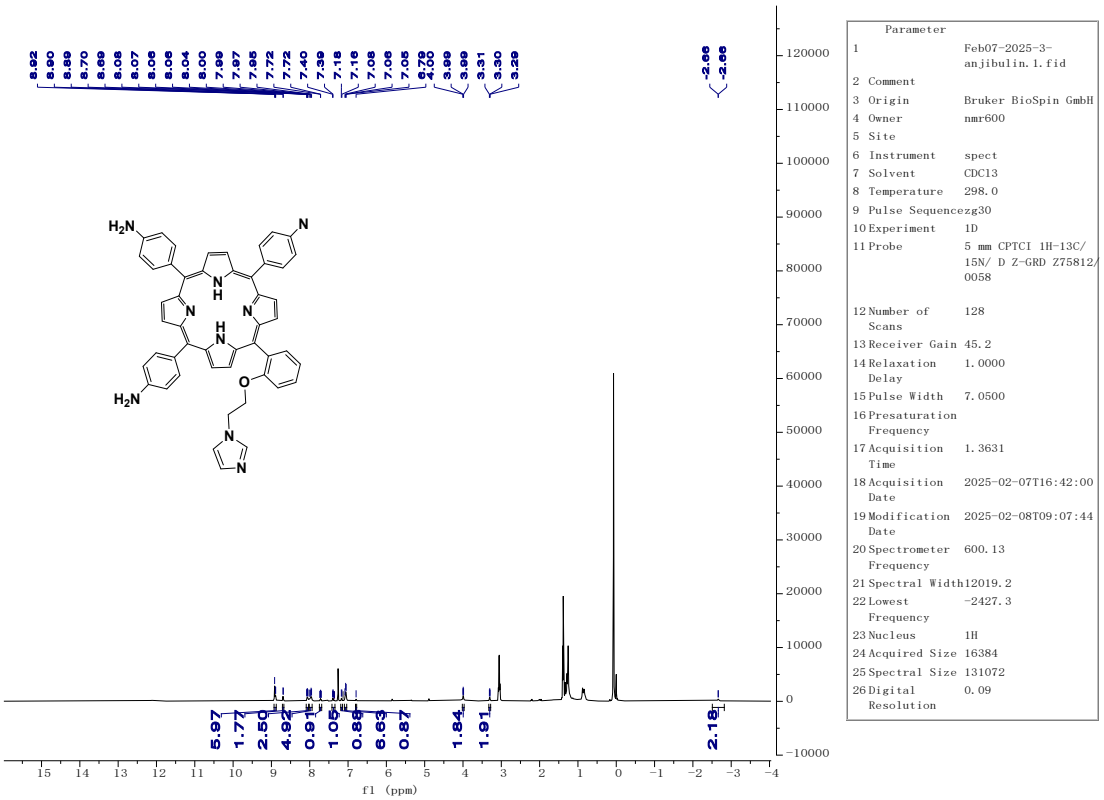

Figure S34. NMR spectrum of TAC_2IPP

Text S5. UV-Vis characterization of side-chain imidazole-modified iron porphyrins

The methyl-substituted porphyrin (C_nIPP) exhibited a Soret band at 418 nm and characteristic Q-bands at 515 nm, 550 nm, 592 nm, and 647 nm, consistent with the typical optical signature of porphyrins. In contrast, the amino-substituted porphyrin (TAC_2IPP) displayed a Soret band at 435 nm, along with Q-bands at 527 nm, 575 nm, and 665 nm. Upon iron coordination, FeC_nIPP retained a Soret band centered at 418 nm, albeit broader, while only the Q-band near 508 nm remained prominent, accompanied by a shoulder peak at 378 nm. $FeTAC_2$IPP, however, exhibited a significantly broadened and blueshifted Soret band, along with the complete disappearance of Q-bands. These distinct spectral changes confirm the successful formation of iron-porphyrin coordination complexes.

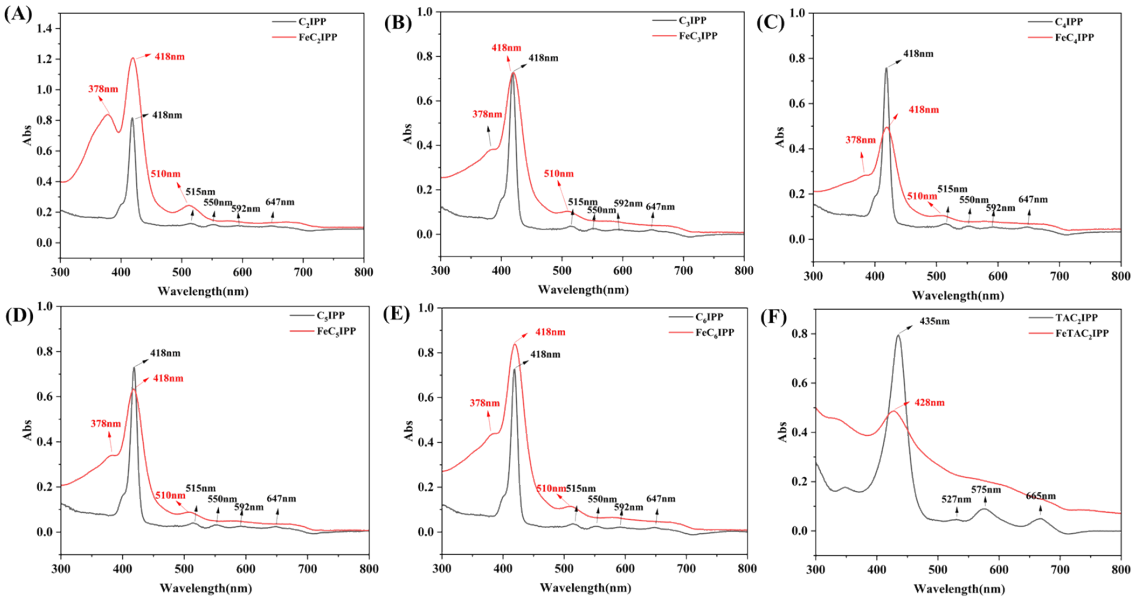

Figure S35. (A) Ultraviolet map of C2IPP and FeC2IPP, (B) Ultraviolet map of C3IPP and FeC_3IPP, (C) Ultraviolet map of C_4IPP and FeC_4IPP, (D) Ultraviolet map of C_5IPP and FeC_5IPP, (E) Ultraviolet map of C_6IPP and FeC_6IPP, (F) Ultraviolet map of TAC_2IPP and $FeTAC_2$IPP

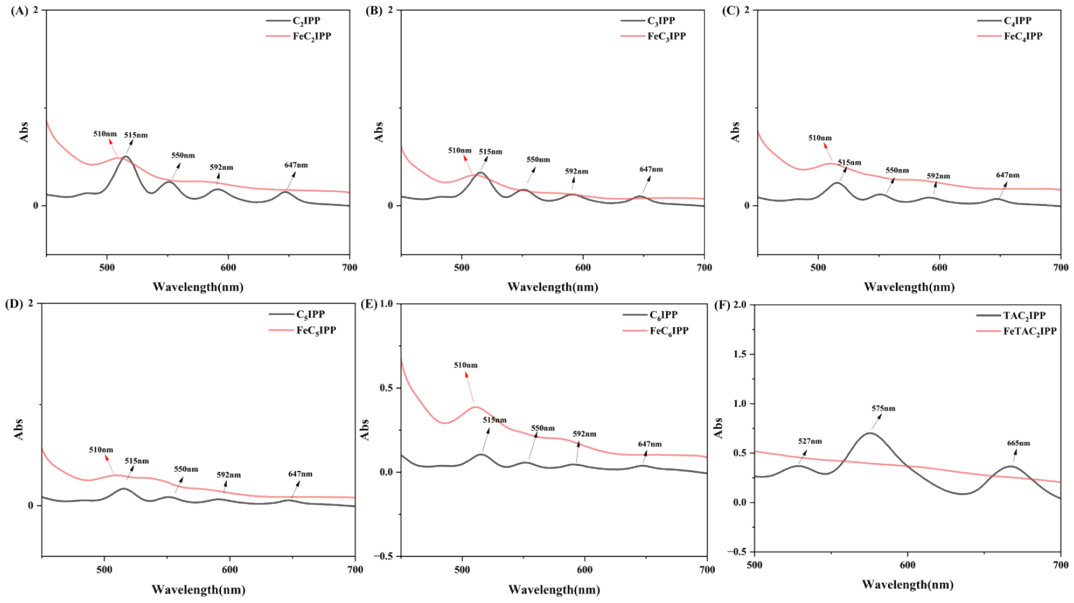

Figure S36. (A) Q-band map of C_2IPP and FeC_2IPP, (B) Q-band map of C_3IPP and FeC_3IPP, (C) Q-band map of C_4IPP and FeC_4IPP, (D) Q-band map of C_5IPP and FeC_5IPP, (E) Q-band map of C_6IPP and FeC_6IPP, (F) Q-band map of TAC_2IPP and FeTAC_2IPP

Text S6. XPS characterization of side-chain imidazole-modified iron porphyrins

X-ray photoelectron spectroscopy (XPS) was applied to analyze the six newly synthesized iron porphyrin catalysts. Results demonstrate that the Fe 2p spectra of these catalysts consist of two characteristic peaks: Fe $2p_{3/2}$ (710.2–711.6 eV) and Fe $2p_{1/2}$ (723.3–725.0 eV). These values align well with the literature's typical binding energy range for Fe^{3+} (Fe $2p_{3/2}$ about 710 –712 eV, Fe $2p_{1/2}$ about 723–725 eV) [8, 9]. This consistency confirms the presence of iron in the +3 oxidation state within the synthesized iron porphyrins, thereby validating the synthesis's success(**Figure S34A**).

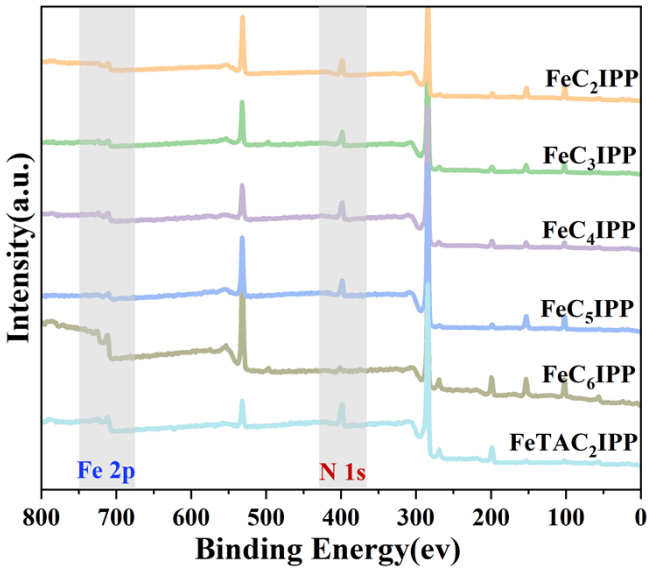

Figure S37. XPS profile of novel iron porphyrin

Table S2. Elemental analysis of iron porphyrin catalyst by CHN analysis

Iron porphyrin	Carbon %		Hydrogen %		Nitrogen %	
	calculate	found	calculate	found	calculate	found
FeC_2IPP	72.94%	72.87%	4.71%	4.72%	9.82%	9.81%
FeC_3IPP	73.15%	73.02%	4.86%	4.79%	9.66%	9.66%
FeC_4IPP	73.35%	73.29%	5.02%	5.05%	9.50%	9.47%
FeC_5IPP	73.54%	73.55%	5.16%	5.13%	9.36%	9.34%
FeC_6IPP	73.72%	73.68%	5.30%	5.37%	9.21%	9.08%
$FeTAC_2IPP$	68.50%	68.62%	4.34%	4.22%	14.67%	14.73%

Table S3. Exploration of the catalytic activity of novel iron porphyrins

Entry	Catalyst	Oxidant	Solvent	Yield(%)
1	FeTMPP	TBHP	DCM	20.86%
2	FeC_2IPP	TBHP	DCM	44.30%
3	FeC_3IPP	TBHP	DCM	34.36%
4	FeC_4IPP	TBHP	DCM	17.83%
5	FeC_5IPP	TBHP	DCM	34.30%
6	FeC_6IPP	TBHP	DCM	17.95%

The reaction conditions are as follows: 4-bromo-2,6-difluoroaniline (0.25 mmol,

50 mg); iron porphyrin(1.25×10^{-6}mol); tert-butyl hydrogen peroxide (0.75 mmol, 103 μL); methylene chloride (10 mL); and the reaction was carried out at room temperature for 4 hours.

Text S7. Synthesis of graphene oxide(GO)

Using Hummer's method, 400 mL of concentrated sulfuric acid was added to a 2 L flask and stirred in an ice-water bath for 5 minutes. Next, 8 g of graphite powder and 4 g of sodium nitrate were slowly added, and the reaction was continued in the ice-water bath for 30 minutes. Afterward, 28 g of potassium permanganate was slowly added, and the reaction was allowed to proceed in the ice-water bath for an additional 45 minutes. The reaction flask was then transferred to a 35 °C constant-temperature water bath, and stirring was continued for 45 minutes. Following this, 360 mL of deionized water was slowly added, and the reaction was continued for 2 hours. Subsequently, 800 mL of deionized water was added, and a 5% hydrogen peroxide solution was dripped in drop by drop until no bubbles were observed in the solution. After standing stratification, the supernatant was poured off, and the lower substance was washed and filtered with a 5% HCl solution until the filtrate was free of sulfate ions. Finally, the underlying substance was vacuum-dried at 60 °C for 24 hours, resulting in the obtainment of black graphene oxide.

Text S8. Synthesis of GO-$FeTAC_2IPP$

$FeTAC_2IPP$ (0.087 mmol), GO (0.35 g), dicyclohexylcarbodiimide (0.97 mmol), 1-hydroxybenzotriazole (2.22 mmol), and 125 mL of DMF solvent were added to a 250 mL single-neck flask[10]. After sonication for 30 minutes, the mixture was thoroughly stirred. The flask was then placed in an oil bath and heated to 80°C for 4 days. Afterward, the reaction was terminated, and the composite material was collected. The

material was suction-filtered and washed sequentially with deionized water, dichloromethane, and ethanol, with each step repeated 3–5 times. Finally, the composite material was dried under vacuum to obtain the final product.

Text S9. Fixed-capacity detection method of GO-FeTAC$_2$IPP

We used an external standard method to calibrate a standard curve and formulate DMF solutions of FeTAC$_2$IPP with concentrations of 6.25 ppm, 12.50 ppm, 25.00 ppm, 50.00 ppm, and 100.00 ppm. By measuring the absorbance of these solutions at 424 nm, we obtained the standard curve equation:(Y=0.0102X+0.0031), where Y represents the absorbance and X represents the concentration of FeTAC$_2$IPP. The high coefficient of determination (R^2 = 0.9968) indicates that the standard curve exhibits excellent linear correlation, ensuring a high degree of confidence in the measurements. Subsequently, the absorbance of the filtered 200 mL filtrate was measured and found to be 0.83. Using the standard curve, the adsorption capacity of GO-FeTAC$_2$IPP was calculated to be 0.10 g/g.

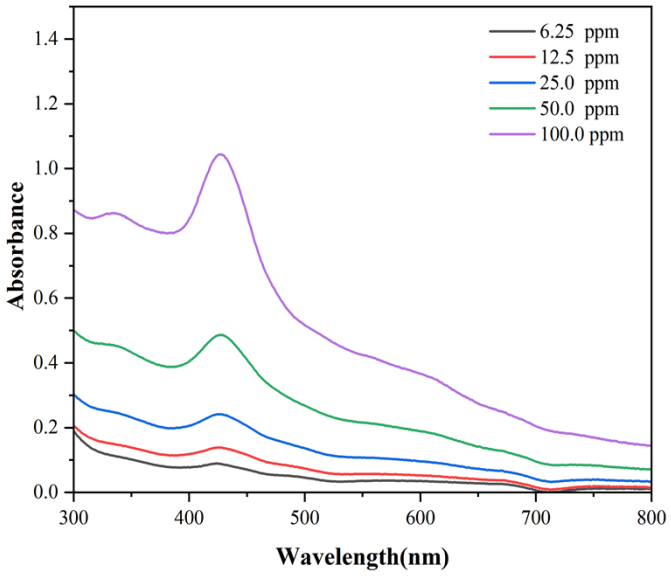

Figure S38. Absorbance of different concentrations of FeTAC$_2$IPP

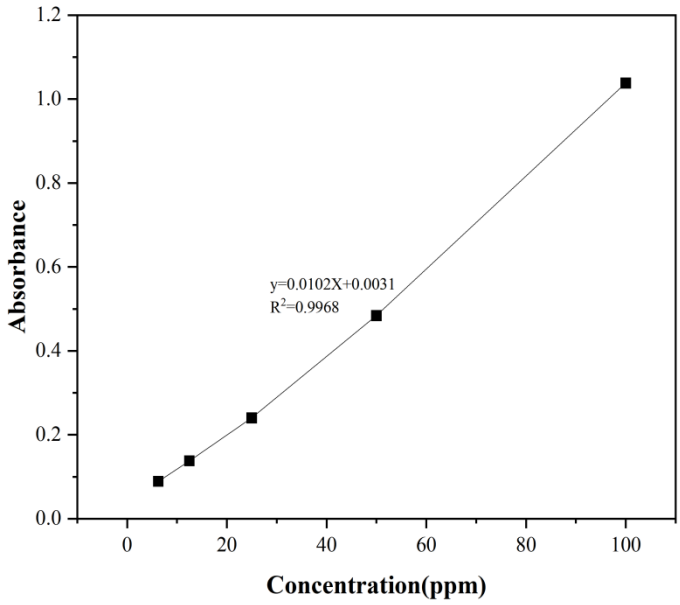

Figure S39. Standard curve equation plot of $FeTAC_2IPP$

Text S10. Infrared characterization of GO-$FeTAC_2IPP$

Fourier transform infrared spectroscopy (FTIR) was performed to characterize the graphene oxide (GO). The prominent absorption bands observed at 3419 cm^{-1} correspond to the stretching vibration of the hydroxyl (-OH) groups. Additionally, the peak at 1624 cm^{-1} is indicative of the carbon-carbon double bond (-C=C-) stretching, and the bands at 1411 cm^{-1} and 1213 cm^{-1} are characteristic of the carbonyl (-C=O) and carbon-oxygen (-C-O-) bonds, respectively. These spectral features collectively confirm the successful synthesis and characterization of graphene oxide [11-13]. Furthermore, the FTIR spectrum of the GO-$FeTAC_2IPP$ composite reveals a characteristic peak at 1632 cm^{-1}, corresponding to the amide bond (-CO-NH-) [14-17], which provides additional evidence of the successful integration of GO with $FeTAC_2IPP$.

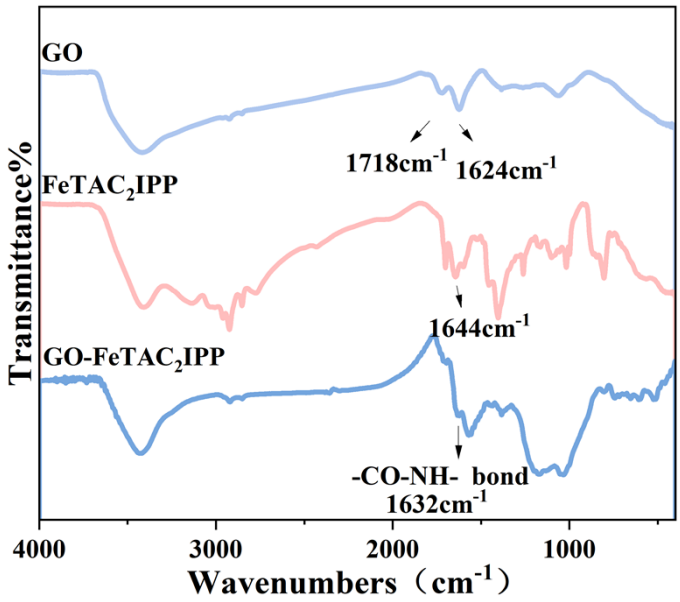

Figure S40. Infrared spectrum of GO, $FeTAC_2IPP$, and GO-$FeTAC_2IPP$

Text S11. XPS characterization of GO-$FeTAC_2IPP$

XPS analysis further revealed that graphene oxide (GO) lacks significant peaks in the Fe 2p and N 1s regions, indicating the absence of Fe and N elements in its structure. Conversely, the GO-$FeTAC_2PP$ composites exhibit prominent peaks in the Fe 2p region at 400.0 eV, 711.66 eV, and 724.6 eV. These peaks correspond to those of the original $FeTAC_2PP$ catalyst, confirming the successful incorporation of iron and the successful synthesis of the GO-$FeTAC_2PP$ composite material.

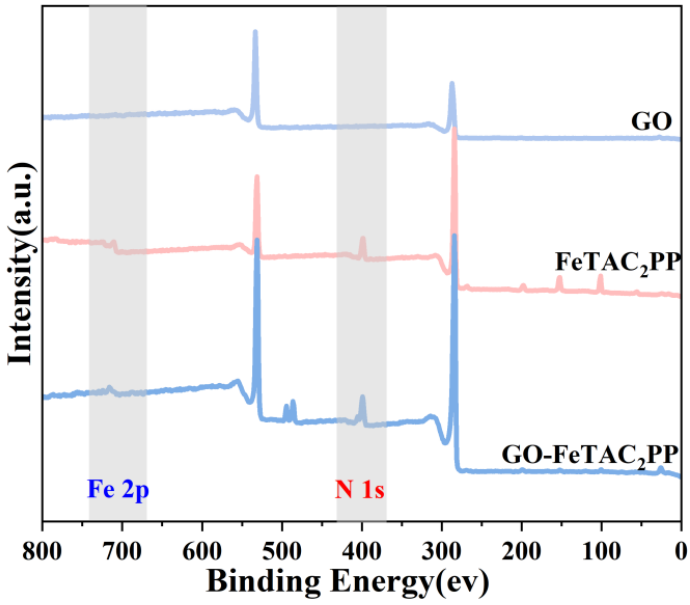

Figure S41. XPS profile of GO, $FeTAC_2IPP$, and GO-$FeTAC_2IPP$

Text S12. XRD characterization of GO-$FeTAC_2IPP$

The XRD analysis revealed a characteristic diffraction peak of graphene oxide (GO) at 2θ = 11.46°, corresponding to a layer spacing of 0.78 nm [18-20]. When GO covalently bonds with $FeTAC_2IPP$ to form GO-$FeTAC_2IPP$ composites, a new diffraction peak emerges at 2θ = 10.88°, indicating an increased layer spacing of 0.83 nm. This increase confirms the successful binding of $FeTAC_2IPP$ molecules to GO and highlights the modification in the interlayer structure of the composite material[21].

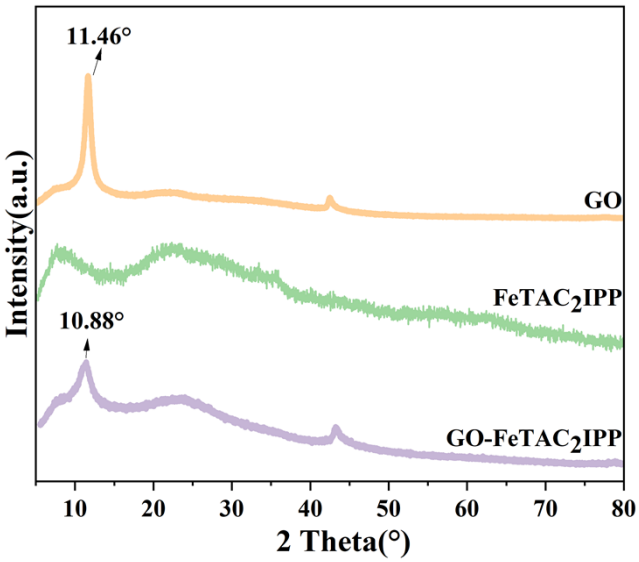

Figure S42. XRD profiles of GO, $FeTAC_2IPP$, and GO-$FeTAC_2IPP$; Measurements were performed using a MiniFlex 600 diffractometer with Cu Kα radiation (λ = 1.5406 Å) at 36 kV and 30 mA, with a scanning rate of 8°/min over the 2θ range of 5-80° (step size 0.02°).

Text S13. SEM characterization of GO-$FeTAC_2IPP$

Scanning electron microscopy (SEM) analysis revealed that graphene oxide (GO) exhibited a typical layered structure with folds and irregularities resulting from surface oxidation (**Figure S40A**). Further SEM observations (**Figure S40B**) showed that the surface of GO-$FeTAC_2IPP$ was rougher than that of pure GO, indicating the successful attachment of $FeTAC_2IPP$ to the GO surface[22]. Additionally, elemental distribution maps obtained through SEM combined with energy-dispersive X-ray spectroscopy (EDS) (**Figure S40C-D**) demonstrated that Fe and N elements were absent in GO but were evenly distributed in GO-$FeTAC_2IPP$. This further confirmed the successful synthesis of the GO-$FeTAC_2IPP$ immobilized material with favorable properties.

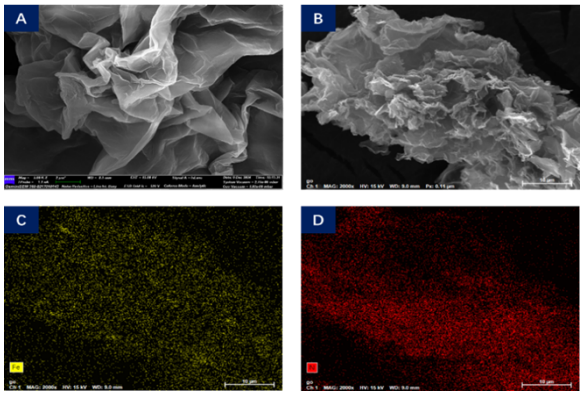

Figure S43. (A) SEM profile of GO, (B) SEM profile of GO-FeTAC$_2$IPP, (C) EDS profile of GO-FeTAC$_2$IPP (Fe), (D) EDS profile of GO-FeTAC$_2$IPP (N)

Text S14 TGA characterization of GO-FeTAC$_2$IPP

Thermogravimetric analysis (TGA) revealed that graphene oxide (GO) lost 5% of its weight between 30°C and 200°C, primarily due to the evaporation of adsorbed water or volatile substances. From 200°C to 250°C, an additional 19% weight loss occurred, attributable to the decomposition of oxygen-containing functional groups. Above 250°C, the weight loss rate of GO slowed significantly, with a total mass loss of 33% at 600°C. In contrast, FeTAC$_2$IPP exhibited moderate thermal stability at high temperatures, but its weight loss reached 40% at 600°C, likely due to the degradation of its side-chain carbon structures under thermal stress. Notably, the thermal stability of the GO-FeTAC$_2$IPP composite was markedly enhanced. For GO-FeTAC$_2$IPP, the initial weight loss (30°C–150°C) was dominated by water evaporation, similar to pure GO. However, in the 200°C–250°C range, the composite demonstrated a slower weight loss rate compared to pristine FeTAC$_2$IPP, suggesting that GO-FeTAC$_2$IPP interactions improved thermal resistance. By 600°C, the total weight loss of GO-FeTAC$_2$IPP was significantly lower than that of FeTAC$_2$IPP alone (33% vs. 40%), confirming that GO effectively stabilized the composite. These results demonstrate that GO-FeTAC$_2$IPP exhibits superior thermal stability at elevated temperatures, owing to both the intrinsic

stabilizing effect of GO and its synergistic interactions with $FeTAC_2IPP$.

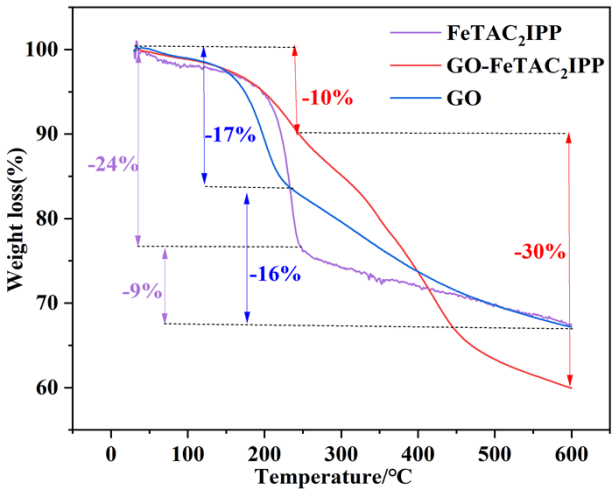

Figure S44 TGA profiles of GO, $FeTAC_2IPP$, and GO-$FeTAC_2IPP$

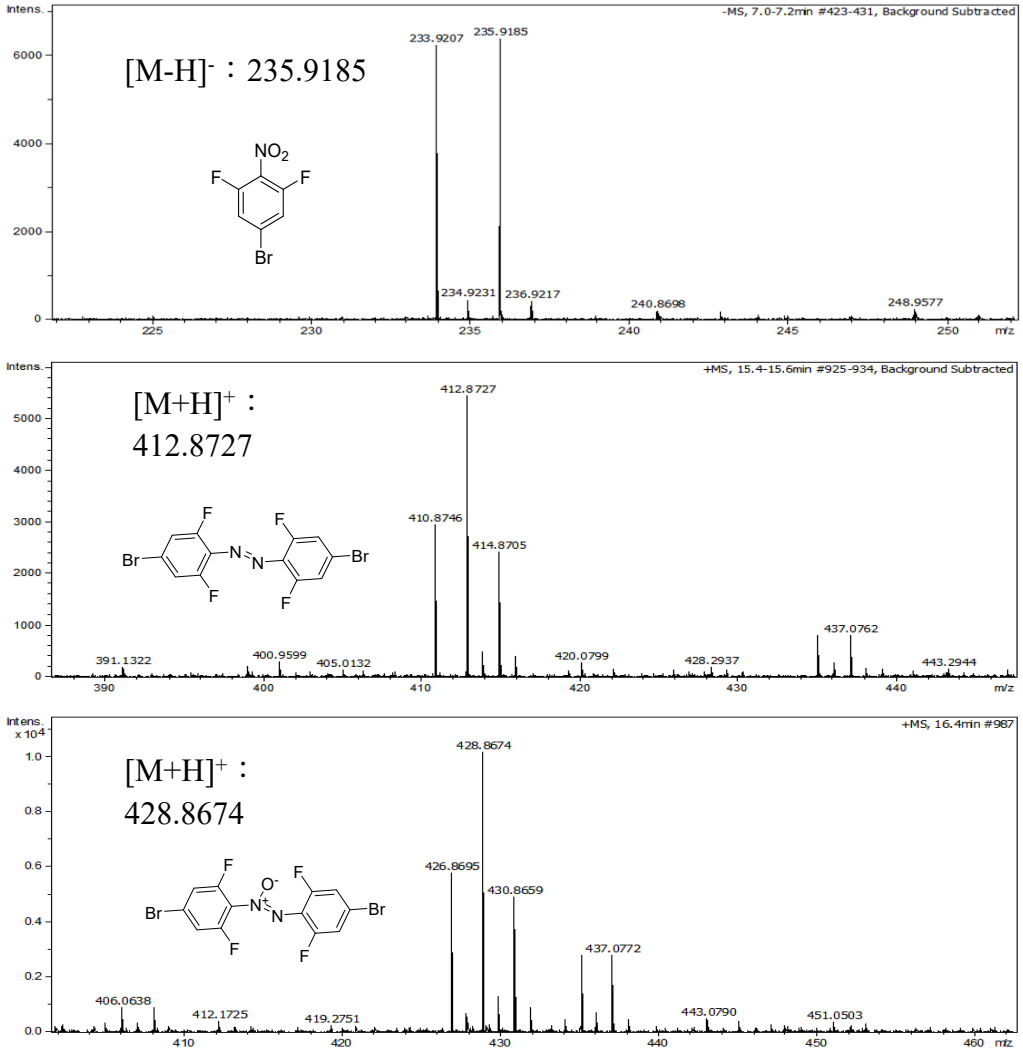

Figure S45. Impurity mass spectra

References

[1] V. Sol, A. Charmot, P. Krausz, S. Trombotto, Y. Queneau, Synthesis of new glucosylated porphyrins bearing an α-d-linkage, Journal of Carbohydrate Chemistry, 25(2006) 345-360.

[2] V. Chaleix, V. Sol, Y. M. Huang, M. Guilloton, R. Granet, J. C. Blais, P. Krausz, RGD-porphyrin conjugates: synthesis and potential application in photodynamic therapy, European Journal of Organic Chemistry, 2003(2003) 1486-1493.

[3] R. Li-Lei, P. Xiao-Xia, W. Shu-Jun, X. Li-Wei, L. Ze-Qiang, Syntheses, Spectral and Electrochemical Properties, Antitumor Activities of Manganese/Zinc Complexes with Porphyrin Modified by 5-Fluorouracil, Chinese Journal of Inorganic Chemistry, 35(2019) 965-970.

[4] L. Xie, X. P. Zhang, B. Zhao, P. Li, J. Qi, X. Guo, B. Wang, H. Lei, W. Zhang, U. P. Apfel, Enzyme-inspired iron porphyrins for improved electrocatalytic oxygen reduction and evolution reactions, Angewandte Chemie, 133(2021) 7654-7659.

[5] D. Feng, Z. Y. Gu, J. R. Li, H. L. Jiang, Z. Wei, H. C. Zhou, Zirconium-metalloporphyrin PCN-222: mesoporous metal–organic frameworks with ultrahigh stability as biomimetic catalysts, Angewandte Chemie-International Edition, 51(2012) 10307.

[6] H. B. Fa, L. Zhao, X. Q. Wang, J. H. Yu, Y. B. Huang, M. Yang, D. J. Wang. Chiral Recognition of Mesoporous SBA-15 with an Incorporated Chiral Porphyrin [Z]. Wiley Online Library. 2006

[7] S. Meng, Z. Xu, G. Hong, L. Zhao, Z. Zhao, J. Guo, H. Ji, T. Liu, Synthesis, characterization and in vitro photodynamic antimicrobial activity of basic amino acid–porphyrin conjugates, European Journal of Medicinal Chemistry, 92(2015) 35-48.

[8] J. Conradie, E. Erasmus, XPS Fe 2p peaks from iron tris (β-diketonates): Electronic effect of the β-diketonato ligand, Polyhedron, 119(2016) 142-150.

[9] T. Yamashita, P. Hayes, Analysis of XPS spectra of Fe2+ and Fe3+ ions in oxide materials, Applied Surface Science, 254(2008) 2441-2449.

[10] A. Lewandowska-Andralojc, E. Gacka, T. Pedzinski, G. Burdzinski, A. Lindner, J. M. O'brien, M. O. Senge, A. Siklitskaya, A. Kubas, B. Marciniak, Understanding structure–properties relationships of porphyrin linked to graphene oxide through π–π-stacking or covalent amide bonds, Scientific Reports, 12(2022) 13420.

[11] S. Stankovich, R. D. Piner, S. T. Nguyen, R. S. Ruoff, Synthesis and exfoliation of isocyanate-treated graphene oxide nanoplatelets, Carbon, 44(2006) 3342-3347.

[12] S. Rayati, S. Rezaie, F. Nejabat, Mn (III)-porphyrin/graphene oxide nanocomposite as an efficient catalyst for the aerobic oxidation of hydrocarbons, Comptes Rendus Chimie, 21(2018) 696-703.

[13] R. Hajian, E. Bahrami, Mn (III)-porphyrin immobilized on the graphene oxide-magnetite nanocomposite as an efficient heterogeneous catalyst for the epoxidation of alkenes, Catalysis Letters, 2022) 1-12.

[14] R. Yamuna, S. Ramakrishnan, K. Dhara, R. Devi, N. K. Kothurkar, E. Kirubha, P. Palanisamy, Synthesis, characterization, and nonlinear optical properties of graphene oxide functionalized with tetra-amino porphyrin, Journal of Nanoparticle Research, 15(2013) 1-9.

[15] A. Zarrinjahan, M. Moghadam, V. Mirkhani, S. Tangestaninejad, I. Mohammadpoor-Baltork, Graphene oxide nanosheets supported manganese (III) porphyrin: a highly efficient and reusable biomimetic catalyst for epoxidation of

alkenes with sodium periodate, Journal of the Iranian Chemical Society, 13(2016) 1509-1516.
[16] M. Keyhaniyan, A. Shiri, H. Eshghi, A. Khojastehnezhad, Synthesis, characterization and first application of covalently immobilized nickel-porphyrin on graphene oxide for Suzuki cross-coupling reaction, New Journal of Chemistry, 42(2018) 19433-19441.
[17] S. Kumar, R. K. Yadav, K. Ram, A. Aguiar, J. Koh, A. J. Sobral, Graphene oxide modified cobalt metallated porphyrin photocatalyst for conversion of formic acid from carbon dioxide, Journal of CO2 Utilization, 27(2018) 107-114.
[18] L. Stobinski, B. Lesiak, A. Malolepszy, M. Mazurkiewicz, B. Mierzwa, J. Zemek, P. Jiricek, I. Bieloshapka, Graphene oxide and reduced graphene oxide studied by the XRD, TEM and electron spectroscopy methods, Journal of Electron Spectroscopy and Related Phenomena, 195(2014) 145-154.
[19] L. Zhang, Y. Li, H. Guo, H. Zhang, N. Zhang, T. Hayat, Y. Sun, Decontamination of U (VI) on graphene oxide/Al2O3 composites investigated by XRD, FT-IR and XPS techniques, Environmental Pollution, 248(2019) 332-338.
[20] F. M. C. Caicedo, E. V. López, A. Agarwal, V. Drozd, A. Durygin, A. F. Hernandez, C. Wang, Synthesis of graphene oxide from graphite by ball milling, Diamond and Related Materials, 109(2020) 108064.
[21] Y. Du, N. Dong, M. Zhang, K. Zhu, R. Na, S. Zhang, N. Sun, G. Wang, J. Wang, Covalent functionalization of graphene oxide with porphyrin and porphyrin incorporated polymers for optical limiting, Physical Chemistry Chemical Physics, 19(2017) 2252-2260.
[22] A. Khojastehnezhad, M. Bakavoli, A. Javid, M. M. Khakzad Siuki, F. Moeinpour, Covalently copper (II) porphyrin cross-linked graphene oxide: Preparation and catalytic activity, Catalysis Letters, 149(2019) 713-722.